JOINT LABORATORY OF OPTICS
FACULTY OF SCIENCE
PALACKÝ UNIVERSITY OLOMOUC

SUMMARY OF THE DOCTORAL THESIS

Forward physics with the ATLAS detector

Design of radiation resistant descendant of the ALFA detector, detector AFP

2018

Ing. Ladislav Chytka

Supervisor: Mgr. Tomáš Sýkora, Ph.D.

Study field: Applied Physics, full-time form

The doctoral thesis was carried out under the full time doctoral program Physics in the specialization Applied Physics in 2012–2018. The research institute at which the thesis was prepared was the Joint Laboratory of Optics in Olomouc. The program was maintained by the Department of Experimental Physics of Faculty of Science at Palacký University in Olomouc.

Ph.D. candidate:	**Ing. Ladislav Chytka**
Supervisor:	**Mgr. Tomáš Sýkora, Ph.D.** Institute of Particle and Nuclear Physics Faculty of Mathematics and Physics Charles University in Prague
Reviewers:	**prof. RNDr. Stanislav Tokár, DrSc.** Department of Nuclear Physics and Biophysics Faculty of Mathematics, Physics and Informatics Comenius University in Bratislava
	prof. Ing. Josef Žáček, DrSc. Institute of Particle and Nuclear Physics Faculty of Mathematics and Physics Charles University in Prague

The summary of the thesis has been sent to distribution on .....

The oral defense in front of the committee for the Ph.D. study program Physics and the specialization Applied Physics will take place on ..... at the Joint Laboratory of Optics, room ....., 17. listopadu 50A, Olomouc.

The doctoral thesis is available in the library at the Faculty of Science of Palacký University.

Bibliografické údaje

Autor:	Ing. Ladislav Chytka
Název práce:	Dopředná fyzika na detektoru ATLAS (Návrh radiačně odolného následovníka detektoru ALFA, detektor AFP)
Typ práce:	disertační práce
Pracoviště:	Společná laboratoř optiky, Přírodovědecká fakulta, Univerzita Palackého v Olomouci
Rok:	2018
Studijní obor:	Aplikovaná fyzika, prezenční forma
Vedoucí práce:	Mgr. Tomáš Sýkora, Ph.D.
Konzultanti:	RNDr. Karel Černý, Ph.D.
	Mgr. Libor Nožka, Ph.D.
Počet stran:	180
Přílohy:	1 CD/DVD
Jazyk práce:	anglický

Bibliograhic info

Author:	Ing. Ladislav Chytka
Title:	Forward physics with the ATLAS detector (Design of radiation resistant descendant of the ALFA detector, detector AFP)
Thesis type:	doctoral thesis
Department:	Joint Laboratory of Optics, Faculty of Science, Palacký University Olomouc
Year:	2018
Study field:	Applied Physics, full-time form
Supervisor:	Mgr. Tomáš Sýkora, Ph.D.
Advisors:	RNDr. Karel Černý, Ph.D.
	Mgr. Libor Nožka, Ph.D.
Page count:	180
Supplements:	1 CD/DVD
Thesis language:	English

Anotace

Dopředné detektory experimentů na urychlovačích částic umožňují detekovat a měřit částice vystupující ze srážky pod velmi malými úhly, které jsou zajímavé např. pro měření difrakčních procesů, při kterých nedojde k disociaci jedné nebo obou částic vstupující do srážky. Neustále se zvyšující luminozita v urychlovačových experimentech vede ke zvyšování počtu srážek, ke kterým dojde během jedné interakce dvou protiběžných shluků srážených částic. Pro rozlišení bodu, ze kterého pochází částice detekované dopřednými detektory, je proto nezbytný systém pro měření času letu detekovaných částic. Předkládaná práce čtenáři představí experiment ATLAS, jeho dopředné detektory a vybraná témata dopředné fyziky, shrnuje autorovu práci na simulacích dopředných detektorů experimentu ATLAS a dokumentuje autorovo přispění k vývoji systému měření času letu pro detektor AFP s časovým rozlišením pod 30 ps.

Synopsis

Forward detectors of high energy collider experiments allow to tag and measure remnants of a colliding particle moving in a very forward direction that are of interest e.g. for measurements of diffractive processes, where one or both colliding particles are not dissociated and continue in the forward direction. Ever increasing luminosity in collider experiments leads to increased pileup of interactions and a time-of-flight system is necessary for forward detectors in order to determine the primary interaction vertex of recorded particles. The presented work introduces the ATLAS experiment, its forward detectors and selected topics of forward physics, summarizes author's work on simulation of the ATLAS forward detectors and documents authors contribution to the development of AFP time-of-flight system with sub-30 ps time resolution.

Klíčová slova: čas letu; Čerenkovovo záření; MCP-PMT; SiPM; AFP; ATLAS; dopředná fyzika; difrakce v částicové fyzice

Keywords: time-of-flight; Cherenkov light; MCP-PMT; SiPM; AFP; ATLAS; forward physics; diffraction in high energy physics

Contents

Introduction

Forward detectors of high energy collider experiments allow to tag and measure remnants of a colliding particle propagating in the very forward direction, i.e. at very small angles with respect to the circulating beam. Such remnants are of interest e.g. for measurements of diffractive processes, where one or both colliding particles are not dissociated and continue in the forward direction. Especially in the case of the elastic scattering, important for the measurements of total interaction cross section, the forward detectors are of essence.

The presented thesis documents author's contributions to the project of ATLAS forward detectors and to the development of AFP time-of-flight detectors in particular:

1. Software development within the Athena framework of the ATLAS collaboration.

2. Simulation and analysis of forward physics processes potentially interesting for ALFA and AFP detector groups.

3. Participation in beam tests, data taking and analyses.

The first part introduces the LHC, ATLAS and its forward detectors, and gives an overview of accelerator and particle physics related to the measurements with the forward detectors. Necessary concepts of forward physics as well as notations used within the ATLAS collaboration are explained.

The second part covers the simulations. Following the work started in my diploma thesis, I extended and further validated the model of the ATLAS forward region for the use in the full Geant4 based simulation under the Athena framework. The Roman pot filler, serving to reduce the radio-frequency heating of the ALFA stations, was implemented into the ALFA model and the influence of the ATLAS central magnetic field on the ALFA measurement was evaluated. For the AFP, the effect of multiple scattering and hadronic showers due to a thin entrance window was studied.

The third and final part follows my trail in the development of the AFP time-of-flight (ToF) detector. The AFP ToF detector is introduced along with its components. Large part is devoted to beam tests and laboratory testing, where the performance of the developing ToF detector was evaluated. Finally, the ToF installation and commissioning in 2017 is described.

Chapter 1

Forward Physics with the ATLAS detector

1.1 ATLAS and its forward detectors

A Toroidal LHC Apparatus (ATLAS) [1] is a general purpose high energy physics experiment and one of the four large experiments at the Large Hadron Collider (LHC) at the European Organization for Nuclear Research (CERN).

The LHC accelerates protons and heavy ions delivered by the Super Proton Synchrotron (SPS) and brings them to collisions at its four interaction points (IPs). There are two beams circulating in the LHC — clockwise and anticlockwise — with a separate beam pipe for each of them all around the LHC ring, except for the IPs, where the two opposite-going beams share a common pipe [2].

The LHC started up in November 2009 and reached half its design *pp* center-of-mass energy and over half its design luminosity, i.e. 7 TeV (i.e. 3.5 TeV per proton) and $6 \cdot 10^{33}\,\mathrm{cm}^{-2}\mathrm{s}^{-1}$, in 2010. The energy increased in early 2012 to 8 TeV and was kept at this level until the first long shutdown (LS1) that started in 2013. The operations resumed in early 2015 at energy of 13 TeV. The nominal luminosity of $1 \cdot 10^{34}\,\mathrm{cm}^{-2}\mathrm{s}^{-1}$ was reached in 2016 and exceeded by a factor of two in 2017. Running at 13 TeV finishes at the end of 2018 followed by a second long shutdown (LS2), after which the nominal energy of 14 TeV should be reached [3, 4].

The two opposite-going beams are passing through each other at the interaction points and the bunches of protons in one beam are crossing bunches from the other beam. Duration of one *bunch crossing* (BX) is 1 ns [2]. The 25 ns bunch spacing in time corresponds to 7.5 m in distance. Therefore, the beams cannot collide head-on during the runs with large number of bunches since the LHC experiments are tens of meters long in the beam direction in order to capture most of the particles emerging from a single interaction point. Hence, there would be several interaction points 7.5 m apart within one experiment and the peripheral IPs would be effectively spoiling measurements of particles coming from the central IP. To avoid this, a *beam crossing angle* is introduced.

The ATLAS was designed to perform measurements of a wide variety of physics processes, ranging from precision measurements of Standard Model parameters to searches for new physics phenomena. The search for the Standard Model Higgs was of a special interest [1].

ATLAS design follows the usual layered structure of high energy physics collider experiments. Each layer consists of a barrel part and two end cap parts, that together ensure that kinematics of particles emerging from the IP are well measured. The structure is shown in Fig. 1.1.

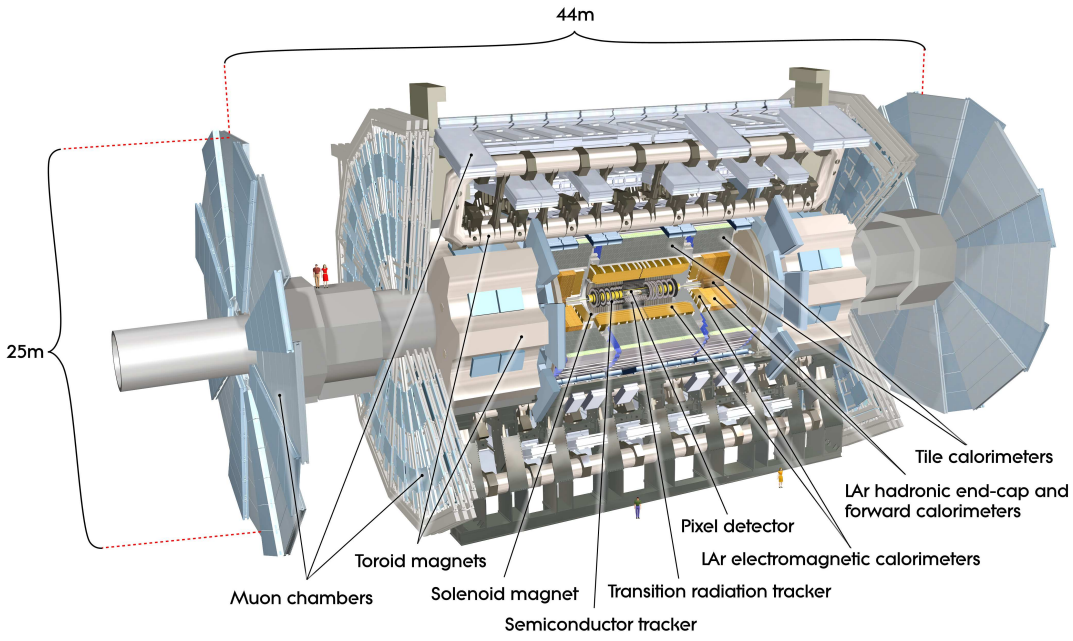

Figure 1.1: ATLAS experiment with a cut out part to see the inner composition of detector layers [1].

The innermost layer of ATLAS is the inner tracker followed by the electromagnetic (EM) calorimeter, the hadronic calorimeter and the muon system. The whole detector is 44 m long and 25 m high.

Apart from the main detector system, ATLAS is also equipped with detectors in the forward region, i.e. downstream from the IP in the direction of both beams. These forward detectors measure particles emerging from the IP at very small angle w.r.t. the beam. There are currently four sets of detectors installed in the forward region — LUCID, ZDC, AFP and ALFA.

The AFP (ATLAS Forward Proton) [5] aims to detect diffractive protons (i.e. protons that are not dissociated in a collision, but loose some energy). It is an upgrade project with the first set of detectors installed in beginning of 2016 and the remaining detectors installed in 2017. AFP detectors are fitted in Roman pot stations placed at 205 and 217 m from the IP on both sides, as illustrated in Fig. 1.2. Each station is instrumented with 4 silicon tracker planes and the stations further from the IP are equipped by a time-of-flight (ToF) system.

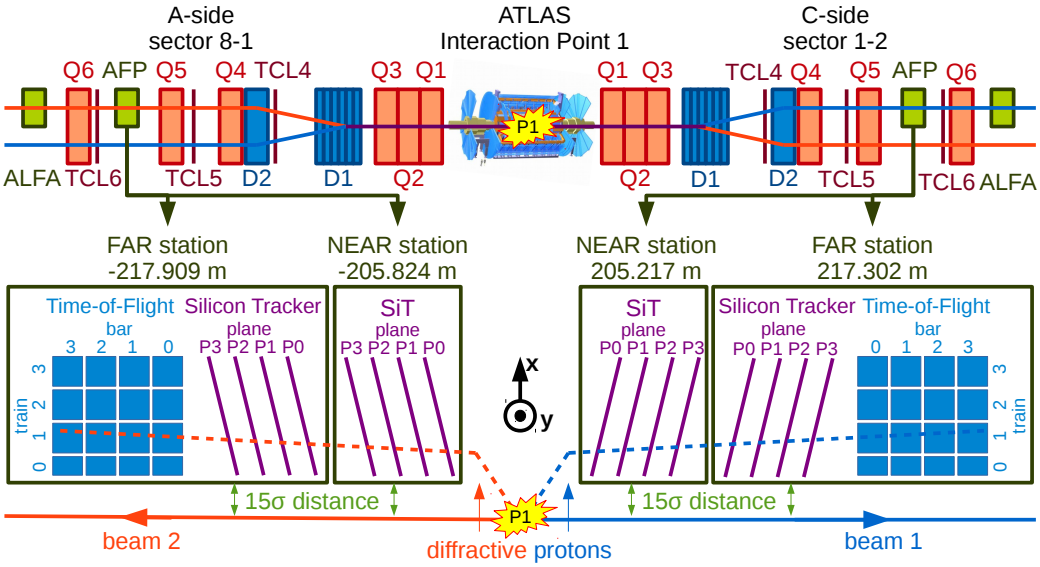

Figure 1.2: Schema of the AFP placement and instrumentation [6].

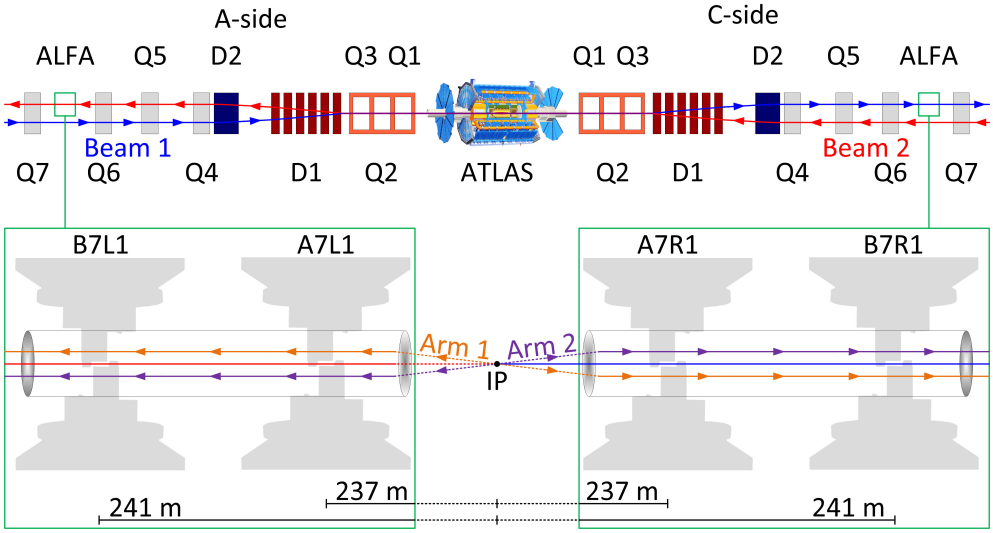

Figure 1.3: Schema of the ALFA placement. The lower part indicates the station names and positions in Run 1 [P11].

ALFA (Absolute Luminosity For ATLAS) [P11] measures tracks of elastic protons in order to determine the luminosity and the total interaction cross section. It utilizes tracking detectors build of cross stacked scintillating fibers read out by multiple anode PMTs (MAPMTs). ALFA consists of four stations located since Run 2 at 237 and 245 m (originally in Run 1 at 241 m) from the IP. Each station houses two Roman pots equipped with detectors placed vertically, above and under the beamline. Roman pots are movable in the vertical direction and can approach the beam closer than 1 mm from the beam center under the

special run conditions. The placement of ALFA stations is illustrated in Fig. 1.3.

1.1.1 ATLAS coordinate system and notation

ATLAS uses right handed Cartesian coordinate system as illustrated in Fig. 1.4, with the origin in the IP, the z axis in the direction of beam, y axis pointing towards surface and x axis oriented to the LHC center. The side with a positive z is called side A and the negative z side is side C [P2, 1].

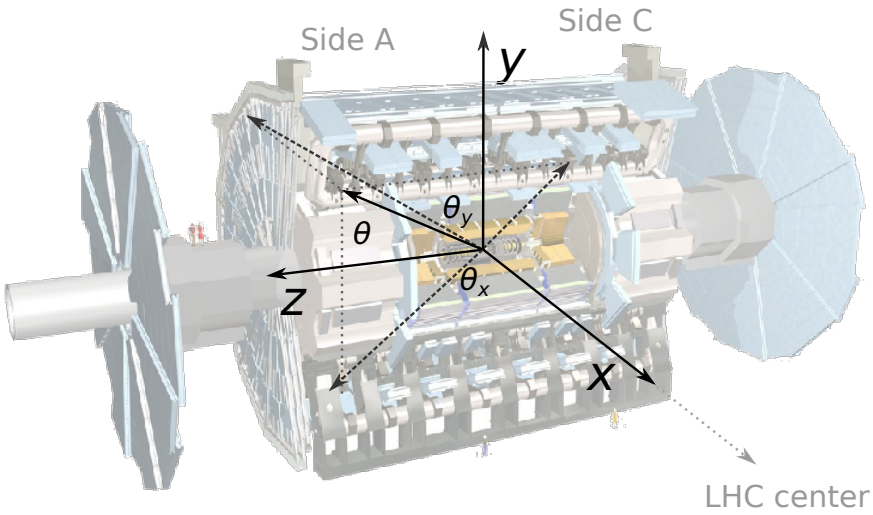

Figure 1.4: ATLAS coordinate system.

The azimuthal angle ϕ is the angle around the beam axis with $\phi = 0$ in the direction of x axis. The polar angle θ is measured from the positive z axis. Apart from the polar angle, pseudorapidity $\eta = -\ln\tan\theta/2$ is commonly used to describe a particle direction w.r.t. the beam axis. It is useful in some cases to replace the polar and azimuthal angles by θ_x, defined as the angle between direction projection to $x-z$ plane and the z axis, and θ_y, being the angle between direction projection to $y-z$ plane and the z axis.

Quantities $\vec{p}_{\mathrm{T}}$, E_{T} and $\vec{E}_{\mathrm{T}}^{\mathrm{miss}}$, i.e. the transverse momentum, transverse energy and transverse missing energy, represent the part of the given physical quantity measured in the $x-y$ plane. The $\vec{p}_{\mathrm{T}}$ is the projection of $\vec{p}$ into the $x-y$ plane, $E_{\mathrm{T}} = \sqrt{m^2c^4 + p_{\mathrm{T}}^2c^2}$ and $\vec{E}_{\mathrm{T}}^{\mathrm{miss}} = -\sum_i \vec{p}_{\mathrm{T},i}$, where $\vec{p}_{\mathrm{T},i}$ is the $\vec{p}_{\mathrm{T}}$ of i-th recorded particle and the sum goes over all visible particles. A quantity often used for description of diffractive events is the fractional momentum loss ξ, defined as $\xi = \frac{p_{\mathrm{z}}^{\mathrm{in}} - p_{\mathrm{z}}^{\mathrm{out}}}{p_{\mathrm{z}}^{\mathrm{in}}}$, where $p_{\mathrm{z}}^{\mathrm{in}}$ is the z component of momentum of the proton before an interaction and $p_{\mathrm{z}}^{\mathrm{out}}$ is the z component of momentum of the proton after the interaction.

The number of interactions within one bunch crossing is distributed according to the Poisson distribution with the average number μ. The μ is used to describe the amount of pileup for specific running conditions.

It is a common practice to label quantities related to the interaction point with a star, e.g. θ_x^* for the θ_x angle under which a particle is emerging from the IP.

Movable detectors in the forward region approach very closely to the beam. Since the beam profile determining the particle flux through such a detector can vary between runs, distance of the detector from the beam (especially the minimal allowed distance) is often given in multiples of the nominal beam width σ_{beam}.

1.2 Forward physics

Forward detectors provide valuable information about a proton or protons that were not dissociated in a collision. This information is of interest especially in case of elastic scattering and diffractive interactions, where zero or only small amount of energy is lost by the protons. Elastic scattering allows to measure total interaction cross section through the optical theorem, while diffraction is useful for probing the proton structure at low momentum transfers.

Both ALFA and the AFP are placed such that there are magnets between them and the IP. ALFA runs with a special magnets setting (so-called *beam optics*) that allows it to determine angles at which protons leave the IP. The AFP can determine the momentum loss ξ from position spread caused by dipole magnets. In both cases, knowledge of beam optics is needed for a successful operation and data analysis.

1.2.1 Elastic and total cross section

The total pp cross section is an important parameter of strong interaction. It is not predicted by the theory, but needs to be measured whenever a higher energy becomes available. Experiments show that it increases with the center-of-mass energy $\sqrt{s}$. Theory predicts so-called Froissart-Martin bound that states that the total cross section cannot rise faster than $\ln^2 s$ [7].

The total cross section can be determined from elastic scattering using the optical theorem from the quantum theory of scattering [P4, 7]

$$\sigma_{\text{tot}} = 4\pi \operatorname{Im} f_{\text{el}}(t)\Big|_{t=0}, \tag{1.1}$$

where $f_{\text{el}}(t)$ is the elastic scattering amplitude and t is the Mandelstam squared four-momentum transfer variable. For small angles, Mandelstam t is related to scattering angle at the IP θ^* as $t \approx -(p\theta^*)^2$, where p is the size of the 3-momentum of the incident proton.

ALFA published measurements of the total cross sections at $\sqrt{s} = 7\,\text{TeV}$ [P5] and at $\sqrt{s} = 8\,\text{TeV}$ [P8] using the luminosity dependent method. The measurement is based on determination of differential elastic cross section $\frac{\mathrm{d}\sigma}{\mathrm{d}t}$ using

measurement of protons positions in ALFA detectors. The measured differential elastic cross section at 8 TeV is plotted in the left part of Fig. 1.5 together with a fit using the theoretical prediction, from which the total cross section and nuclear slope parameter B are extracted.

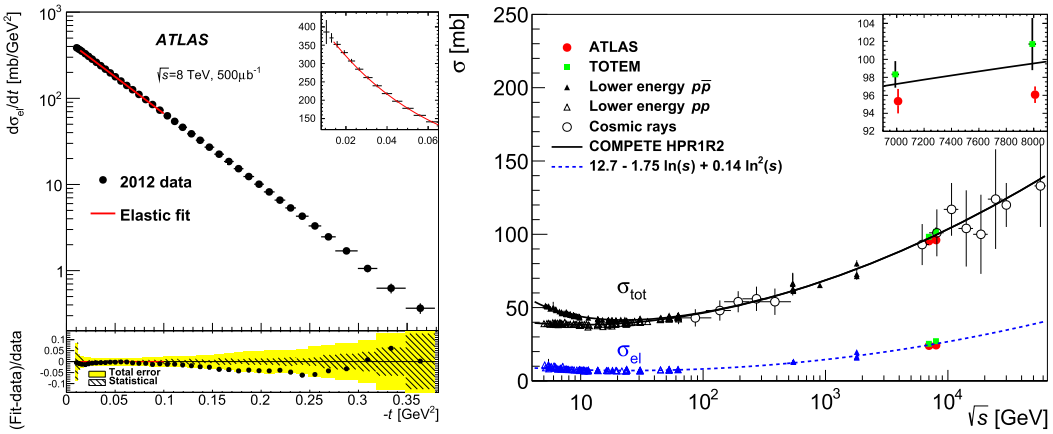

Figure 1.5: *Left:* Differential elastic cross section measured by ALFA with a fit using the theoretical prediction with free parameters σ_{tot} and B. Lower part shows the relative difference between the fit and the data with the yellow area representing the total uncertainty and the hatched area the statistical uncertainty. *Right:* Compilation of total and elastic cross section results as a function of the center-of-mass energy [P8].

Dependence of the total and elastic cross section on the center-of-mass energy is shown in the right part of Fig. 1.5 using data from lower energy pp and $p\bar{p}$ experiments, data from ALFA and TOTEM at 7 TeV and 8 TeV and from cosmic ray observatories.

1.2.2 Diffraction

Diffractive events are characterized by exchange of vacuum quantum numbers ($J^{PC} = 0^{++}$). The incoming protons may be dissociated in the process, but the energy of the outgoing protons, proton and dissociated system, or two dissociated systems is almost equal to that of the incoming protons.

Diffraction in wave optics occurs e.g. when light encounters a black disc. Typical pattern is produced on a distant screen with a forward peak followed by series of minima and maxima. A similar pattern, shown in Fig. 1.6, is observed in the differential cross section $\frac{\mathrm{d}\sigma}{\mathrm{d}t}$ of elastic proton-proton (pp) scattering, where t is again the Mandelstam variable representing squared four-momentum transfer [8].

Depending on the number of dissociated partons, it is possible to classify diffractive events as elastic scattering (no dissociation), single dissociation and double dissociation, as illustrated in Fig. 1.7. A typical sign of a diffractive event is that the outgoing particles are well separated in phase space, mostly observed

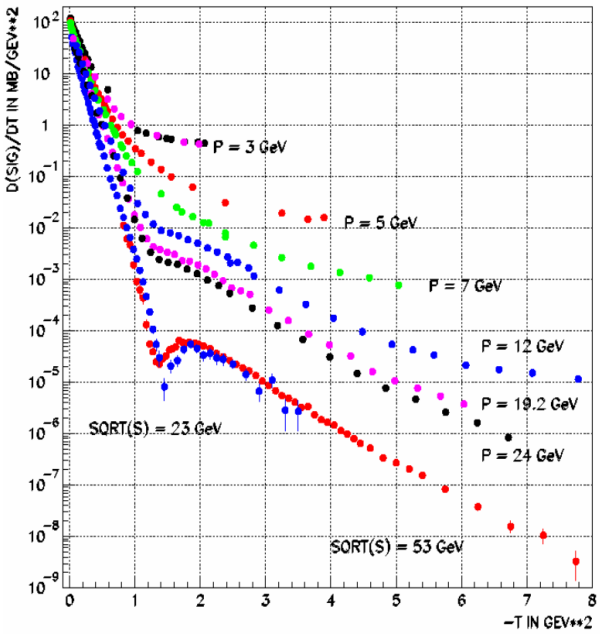

Figure 1.6: Proton-proton elastic cross section as a function of t for various energies in a collision. P stands for momentum of the incoming proton in a fixed target experiment and $\sqrt{s}$ is the center-of-mass energy in pp collision [8].

in a form of a large rapidity gap (LRG). It is also possible to produce particles centrally, such production is called central diffraction.

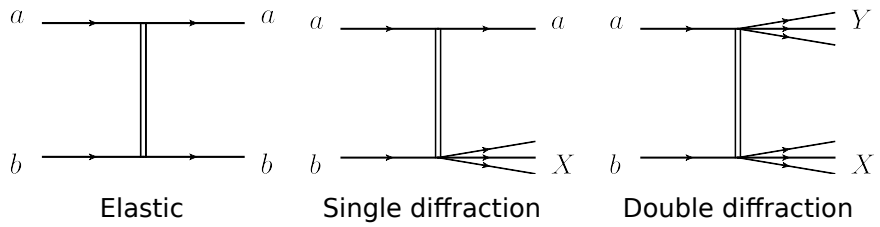

Figure 1.7: Illustration of elastic scattering, single and double diffractive dissociation [5].

There are two distinct regimes in which the diffraction manifests itself. At low momentum transfers, the so-called soft diffraction takes place. Since no hard scale is present, it is not possible to use perturbative quantum chromodynamics (pQCD) and phenomenological models such as Regge theory are used. At high momentum transfers, hard diffraction is observed, with a presence of a hard scale. Hard diffraction can be described using perturbative QCD with pomeron being a compound object represented in the lowest order by a pair of gluons. In this regime, it is possible to measure diffractive parton distribution function (DPDF) of proton and probe the composition of pomeron.

Forward detectors, especially the AFP, provide an additional tag of a proton or protons together with measurement of ξ. Single arm of AFP (the two detectors

on one side of ATLAS forward region) installed in 2016 enabled an extension and an improvement of ATLAS single diffraction (SD) studies, including soft diffraction, SD jet, two jet (jet-gap-jet) and photon+jet production as well as SD W and Z production. The second arm installed in 2017 provided tag of the second outgoing proton, enabling to add central diffraction studies, like DPE production of jets and photon+jet.

Rare processes, like CEP, require much higher statistics, requiring data from high luminosity running. AFP allows to suppress background in such runs by requiring the two tagged protons. Comparison of primary vertex z position reconstructed by inner tracker of ATLAS to the vertex z position calculated from AFP ToF system reduces background by additional factor of up to 10, assuming 10 ps time resolution [9].

The AFP provides a useful tool for background rejection also in other processes with intact protons in the final state. An example of such a process is diphoton scattering or diphoton production of a WW or ZZ pair. Cross sections of such processes depend on the strength of the quartic coupling and therefore it is possible to probe an anomalous quartic coupling predicted by some extensions of the Standard Model. A proton tag (even without ToF information), together with reconstructed bosons, may be sufficient for background suppression, provided that the the anomalous coupling is strong enough [10].

Chapter 2

Simulation of the forward detectors

2.1 Full simulation of the ATLAS forward region

In this chapter, I introduce the packages that allow full Geant4 [11] based simulation of particles entering the very forward region of the ATLAS experiment. Such simulations are useful for the forward detectors of ATLAS. I started the work on the packages already as a part of my master's thesis and I extended the functionality as a part of my ATLAS qualification task. I have documented the packages in an ATLAS note [P7], on which this chapter is based. I omit here the parts describing how to use the code under the Athena framework of ATLAS, as an interested reader can refer to the note [P7] or dedicated TWiki page [P6].

Forward detectors usually use just a mapping tool to calculate particles positions and their momenta at the distance of the detector from the interaction point of ATLAS (IP). Such a tool takes either particles from a particle generator or particles simulated by Geant4 inside of ATLAS volumes and calculates needed positions and momenta using matrices that describe magnets optics in the forward region. Examples of such mapping tools under Athena are `ForwardTransport`, `ForwardTransportFast` [12], `ALFA_BeamTransport` [13], `FPTracker` [14] and `FNTracker` [15] (the later three are now deprecated and replaced by the two former).

I describe here an approach using Geant4 based simulation to transport particles from the IP to the location of a forward detector. There are several advantages of this approach. First, whole simulation runs under Geant4 and therefore simultaneous simulation of multiple forward detectors is naturally possible. Second, also secondary particles emerging in the forward region are simulated. For example, showers developing on beam screens of magnets can be studied. And third, it is possible to move and rotate magnets and vary their fields to study effect of such displacements and field differences. There is also one disadvantage, though — speed. While using e.g. `ForwardTransport` is fast and processing

of thousand events takes a few seconds, using the full simulation is much slower, thousand events on the same computer may take few hours when using the full list of physics processes of Geant4.

The model of the forward region (`ForwardSimulation`) consists of modeled beam pipe elements and the corresponding magnetic fields. It is divided into three packages:

- `ForwardRegionGeoModel` — GeoModel [16] description of the beam pipe elements,
- `ForwardRegionMgField` — magnetic fields definitions for the forward region,
- `ForwardRegionProperties` — the helper C++ class for passing properties from job option to `ForwardRegionMgField`.

Two approaches of description of the beam pipe elements are possible and implemented — GeoModel, implemented by me, and AGDD [17] (Atlas Generic Detector Description), implemented by a CERN summer student Knut Dundas Moraa. The VP1 [18] visualization of the GeoModel implementation is shown in Fig. 2.1.

The description of magnetic fields of magnets in the forward region is provided in the package `ForwardRegionMgField`. Two ways of configuration of the fields are possible — twiss files and `magnets.dat` file. The twiss files contain k_iL values (where k_i is i-th normalized, momentum independent magnetic moment and L is length of the magnet) and magnet lengths, and from these values, B field inductions and induction gradients used by the `ForwardRegionMgField` package are calculated (p_0 is the proton nominal momentum set in the job option file):

$$B_0[\mathrm{T}] = \frac{k_0 p_0[\frac{\mathrm{GeV}}{\mathrm{c}}]}{0.299792458}, \qquad g\left[\frac{\mathrm{T}}{\mathrm{m}}\right] = \frac{k_1 p_0[\frac{\mathrm{GeV}}{\mathrm{c}}]}{0.299792458}. \tag{2.1}$$

The field of the dipoles is described analytically for both D1, D2 and horizontal orbit correctors — $\vec{B} = (0, B_0, 0)$. For the vertical orbit correctors, the perpendicular bending plane is needed — $\vec{B} = (B_0, 0, 0)$. Quadrupole fields are described analytically — $\vec{B} = (gy, gx, 0)$, where g is the field gradient. Originally the inner triplet quadrupole magnets (Q1–Q3) fields were described by measured field maps taken from the FLUKA simulation of ATLAS [19], but this option is now deprecated.

The real LHC magnets are placed with a certain precision and small shifts and rotations occur. In Geant4 based simulation, it is possible to simulate such transformation of fields. In `ForwardSimulation` packages, this feature is implemented for dipole bending magnets D1, D2 and quadrupole magnets Q1–Q7.

I performed several simulations in order to validate the model. First, nominal proton trajectory was checked against MadX [20]. This was shown already in my

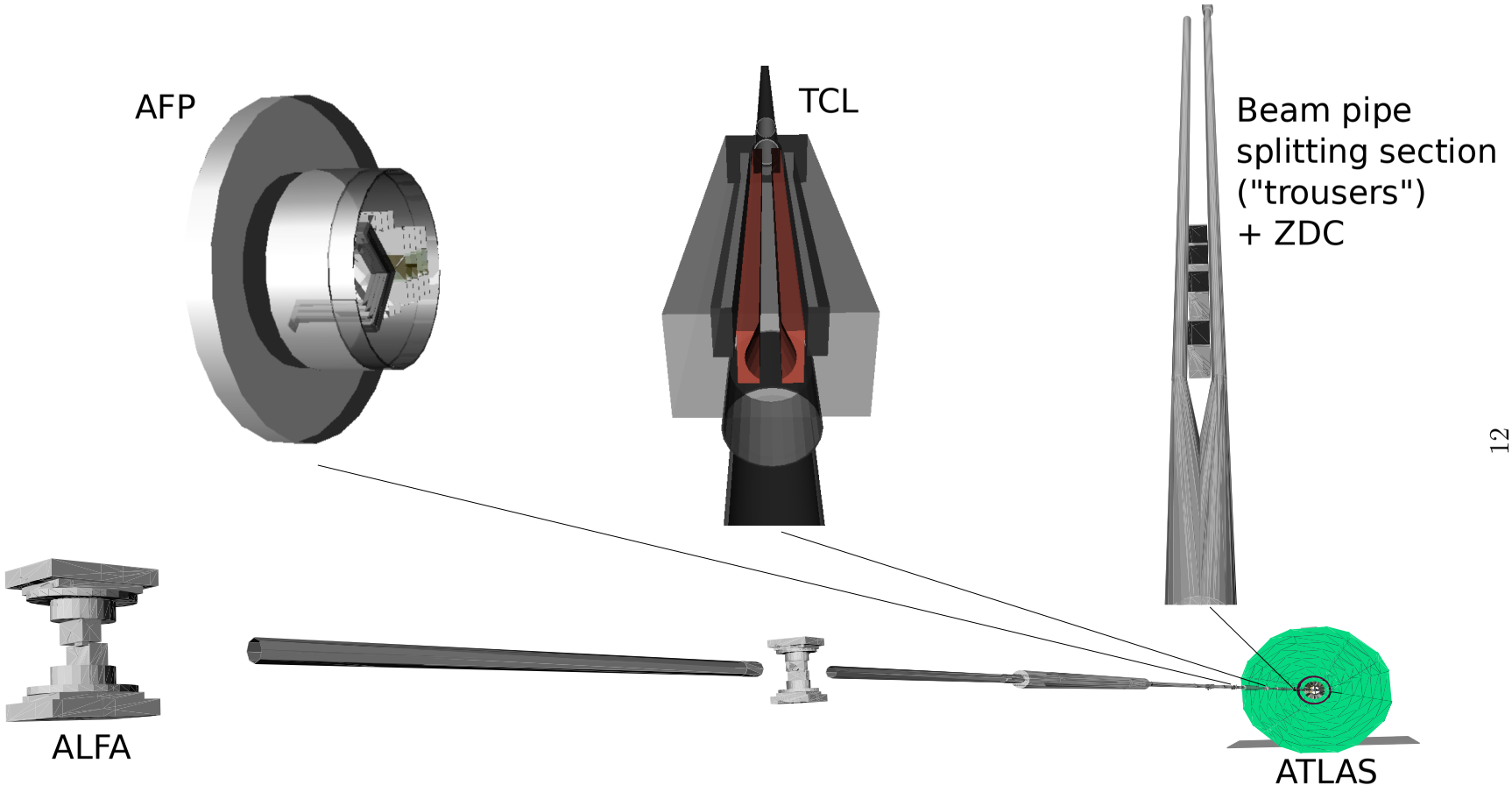

Figure 2.1: Visualization of the forward region model — one side with ALFA, AFP and ATLAS.

master's thesis and the results did not change during later code modifications and extensions. The difference between `ForwardSimulation` and MadX was shown to be less than 0.08 µm [P7].

The results of validation improved for diffractive protons after the extension of the model and several bug fixes. The event-by-event comparison was done again using `ALFA_BeamTransport` and shown a very good agreement with a difference of less than 0.1 µm in x and y coordinate at the ALFA position.

2.2 ALFA simulation

2.2.1 RP filler

The Roman pot fillers installed in all ALFA stations during the LS1 of the LHC were designed to reduce the radio frequency heating of the Roman pots by the proton beam. Each RP filler consists of two copper supports mounted on the preexisting Roman pot and a titanium cylindrical cover with a triangular groove. The cover is equipped with copper-beryllium springs that ensure electrical contact with the existing structure.

I implemented the model of the RP fillers into the GeoModel implementation of the Roman pots under the Athena framework. The model is based on the technical drawings of the RP filler design. The visualization of the RP filler model is shown in Fig. 2.2.

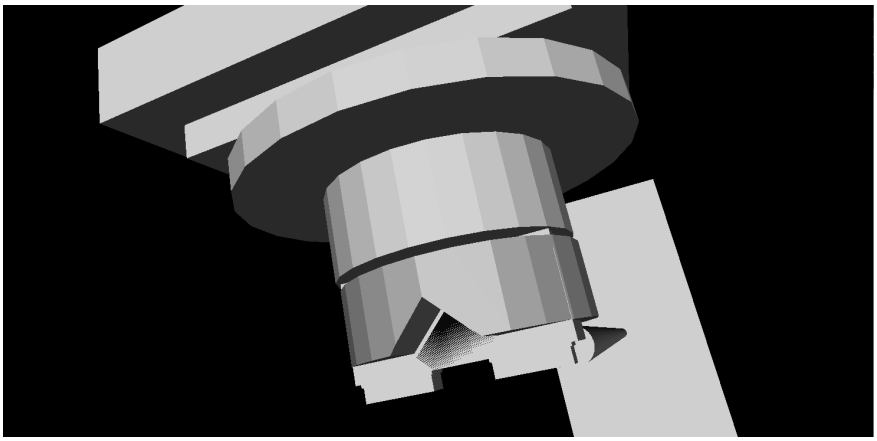

Figure 2.2: VP1 [21] visualization of the ALFA Roman pot (light gray in the foreground) with the RP filler (dark grey).

The model was needed to evaluate the influence of the added material on the ALFA measurements. I produced Monte Carlo samples with and without the RP fillers and the samples were analyzed by CERN summer student Thomas Keck. He shown that while the protons outgoing from the IP are unaffected by the RP fillers, the rate of the secondary particles increases and the energy deposited by the secondaries in the ALFA stations is greater by a factor of 5 [22].

2.2.2 Influence of the ATLAS central magnetic field

Protons leaving ATLAS interaction point in the forward direction are under influence of the magnetic field of the inner tracker solenoid and muon system toroids [1]. I assessed the effect of the ATLAS central magnetic field on measurements of the ALFA detector.

The field effect was evaluated using Monte Carlo (MC) simulation produced in the common ATLAS simulation framework, Athena. A sample of protons going in the forward direction was generated at the ATLAS IP, simulated inside the ATLAS beam pipe, transported or simulated through the Long Straight Section 1 (LSS1) of the LHC until it reached the ALFA detectors and simulated hits were recorded. Each simulation was run twice — once with the magnetic field of ATLAS detector switched on and second with the field switched off.

Several cases were simulated, first, without considering the effect of the ALFA detectors track reconstruction (only recording the precise positions of protons at the end of the ATLAS cavern and right before the first ALFA detector) and second, using the ALFA reconstruction and analysis chain.

The ATLAS magnetic system comprises a solenoid with a 2 T axial magnetic field, a barrel toroid of about 0.5 T and two end-cap toroids with about 1 T field strength. Apart from these active magnets, ferromagnetic structures also affect the total magnetic field of ATLAS.

The fields of the solenoid and the toroids were measured and fitted, and a field map was created based on these measurements by ATLAS magnet systems experts [1]. The field map in the inner detector volume is based only on the fit of the measurement, since the precision is high enough. For the calorimeters and the muon system, calculations and simulations are tuned to the measured points. The complete field map of the ATLAS magnetic field was then produced by connecting all the parts. For more details, see Chap. 2 of the ATLAS overview paper [1]. The field is not ideal due to a non-perfect placement of magnets and the real coil geometry, and the field map accounts for that. Also, the solenoid axis is tilted ($\theta_x = -0.1\,\text{mrad}$, $\theta_y = 0.2\,\text{mrad}$) and shifted ($\Delta x = 0.3\,\text{mm}$, $\Delta y = -2.4\,\text{mm}$, $\Delta z = 0.5\,\text{mm}$) with respect to the axis of the circulating beams (the LHC coordinate system) [23].

First, a simple study was done using protons transported from the IP to the end of ATLAS cavern and to the position of ALFA stations. It showed that the field affects the nominal particles, which results in a shift of order of tens of microns in y direction at the ALFA position. Also a spread in positions was observed of up to 50 microns in the y direction.

After the initial study, I have produced MC samples better corresponding to the real ALFA data, including the ALFA detectors, and I have processed the samples, as much as possible, in the same way as the data from 191373 run. One sample included the central field while the second did not. I have then compared obtained reconstructed positions of tracks in detectors. Here, the comparison of distributions showed a very small difference between the samples, however, comparison on event-by-event basis resulted in 30 to 45 microns RMS difference.

To show, what this means for the ALFA measurement, I have also compared t distributions reconstructed by the subtraction method. Again, the distributions were very much compatible and the event-by-event comparison shown 3 % difference. This value, however, contains also the precision of the reconstruction. Therefore, I have also compared the t values reconstructed by the subtraction method from the true positions of tracks (Fig. 2.3), from which I conclude that the effect of the field on the t measurement of elastic protons is 0.3 %.

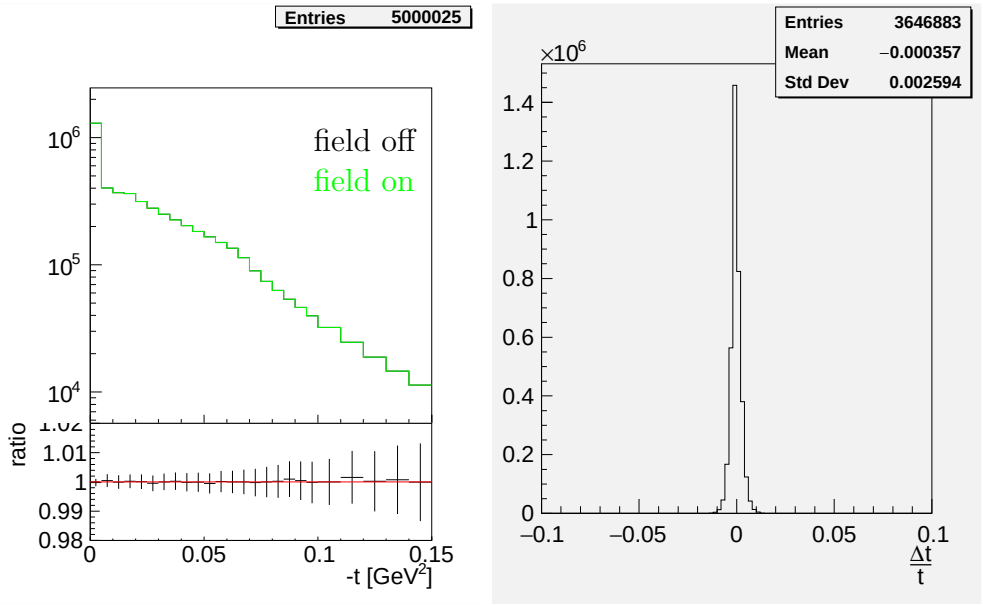

Figure 2.3: Raw t spectrum reconstructed from the true positions of transported protons in the range ALFA uses for fitting. Left: reconstructed t spectrum for both samples without corrections. Right: event-by-event comparison of the reconstructed t for $-t \in [0.05, 0.15)$ GeV^2.

To support the simulation results I attempted to compare the simulation samples and the 191373 run data. Visual distribution agreement is good, but χ^2 tests showed that both samples are not describing the data well enough to draw conclusions about a sample being closer to the data. A discrepancy was found in the resolution of detectors, suggesting that a finer description of the detectors would be needed.

2.3 AFP simulation

The Hamburg beam pipe was considered as a housing for AFP detectors. The initial design offered rectangular detector pockets. Such solution presents a sharp step in aperture to the circulating beam, which leads to RF heating. Therefore, a modification Hamburg beam pipe with angled sides of the detector pockets tilted at the angle of 11° was proposed, as illustrated in Fig. 2.4.

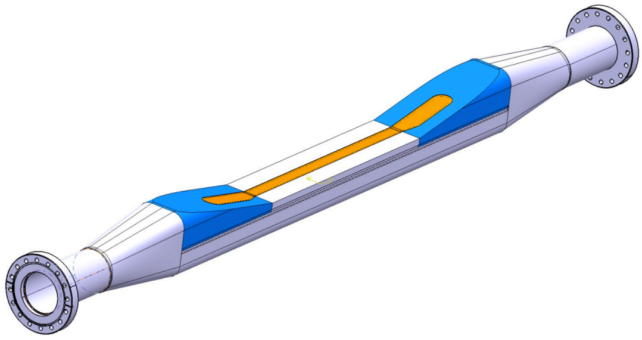

Figure 2.4: Modified Hamburg beam pipe design. The orange area marks the thinned steel window [24].

The tilted pocket wall significantly reduces the RF losses as was demonstrated in simulation [24]. However, the material in the way of the measured diffractive protons is increased. I have performed a set of simulations to evaluate the effect of the added material and hence the scattering of the diffractive protons. The mean value of the scattering angle is evaluated for the two thicknesses and for all the considered angles in Tab. 2.1.

Table 2.1: Mean scattering angle $\langle\theta\rangle$ after the last SiT plane for 0.3 mm and 0.4 mm thick window tilted at angles 11–90°.

	$\langle\theta\rangle$ [µm] for thickness	
Tilt angle [°]	0.3 mm	0.4 mm
11	1.61	1.81
20	1.28	1.43
40	1.03	1.12
60	0.94	1.01
90	0.90	0.96

The added material also increases probability that a hadronic shower develops within the set of detectors in an event. To evaluate how the fraction of events depends on the steel plate tilt, I have rerun the simulation with the default Geant4 physics list enabled and calculated the amount of shower events in each case. The fraction is almost doubled comparing the 90° case to the 11° case with the results of the later being 2.6 % for the 0.3 mm steel and 5.6 % for the 0.4 mm steel.

Chapter 3

Development of the AFP time-of-flight detector

3.1 AFP ToF detector

A good pileup rejection significantly improves ability of the AFP to provide precision measurements for studies of processes described in Sec. 1.2.2. A central diffraction event, like a central exclusive production or a double pomeron exchange, can be mimicked by e.g. two single diffractive interactions occurring simultaneously due to pileup, as illustrated in Fig. 3.1.

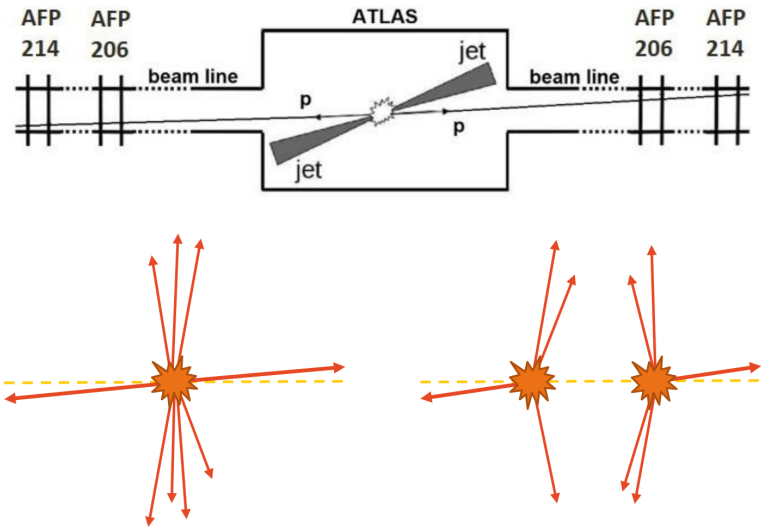

Figure 3.1: Illustration of a central diffraction event and two single diffraction events producing the same signature in AFP.

The two cases — a CD event and two SD events — can be distinguished using the z position of the vertex from which the protons originated. Primary vertices of particles with tracks in ATLAS are reconstructed using the inner tracker. As for the protons, it is possible to determine a difference in time-of-flight of the

two protons Δt using the time-of-flight system installed in the AFP far stations. The protons travel at velocity unmeasurably smaller than the speed of light, therefore, the z position of the vertex can be calculated as $z_{\mathrm{ToF}} = \frac{1}{2}c\Delta t$ and pileup background can be suppressed by matching z_{ToF} to the z positions of vertices reconstructed by the inner tracker.

The current AFP ToF detector was based on QUARTIC [25] with the straight bars replaced by L-shaped bars and original two-inch MCP-PMT by newly available one-inch MCP-PMT.

L-shaped bars, called LQbars, were introduced to fit the ToF detector inside the Roman pot aiming to preserve advantages of QUARTIC, mainly the multiple measurements per proton and the compensation of time of flight for successive bars due to the tilt at Cherenkov angle. LQbars were extensively simulated in Geant4 [11] and further optimizations were introduced that enabled to surpass QUARTIC design performance by 10–40 % [P3].

The AFP ToF is based on the Cherenkov effect — a charged particle traversing a medium at a speed greater than the speed of light in the medium emits light [26]. The emitted light forms a cone with a specific angle between the direction of the particle and that of the emitted photon.

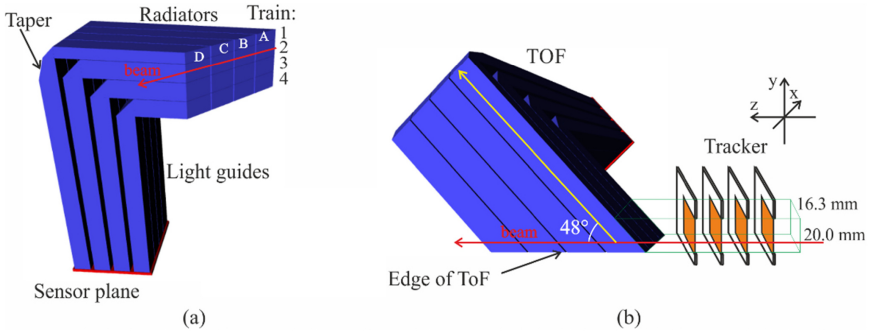

Figure 3.2: (a) Geometry of LQbars assembly in ToF, (b) LQbars with tracker planes (not in scale) [P14].

An LQbar is build from a radiator part and from a light guide part, as is illustrated in Fig. 3.2. The two parts are made of Suprasil (fused silica) glass glued together using Epotek 305 UV transparent epoxy glue [27]. Individual LQbars form 4×4 matrix that is held together with an MCP-PMT in an aluminum or plastic holder. It is customary in the AFP to call four consecutive bars in the proton direction a *train*. Trains are numbered from the bottom of the pot (top part in Fig. 3.2a) towards the light guides. Bars within one train are labeled A–D.

The radiator part is placed at the Cherenkov angle θ_{C} with respect to the incoming protons direction (Fig. 3.2b). The edge of the radiator is cut such that the edge is parallel with the protons. Light guides are rectangular with cross section of $5 \times 6\,\mathrm{mm}^2$ (trains 1–3) and $5.5 \times 6\,\mathrm{mm}^2$ (train 4) given by the MCP-PMT pixel size and the construction of the holder. Radiators thinner than the

light guide have a *taper* at the end towards the radiator as illustrated in Fig. 3.3. The taper straightens a path of significant part of photons that bounce at the walls of the radiator, thus reducing time smearing of the photons arrival [P3].

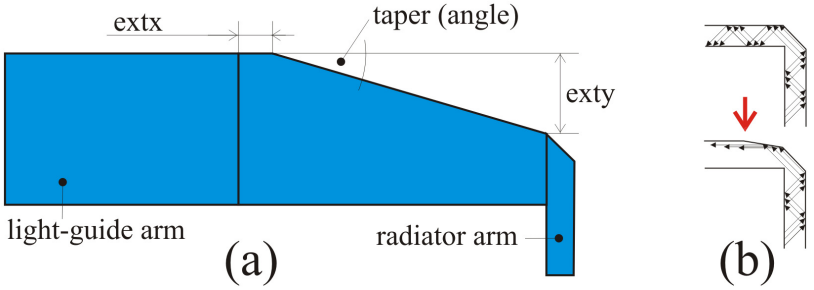

Figure 3.3: Light guide taper [P3].

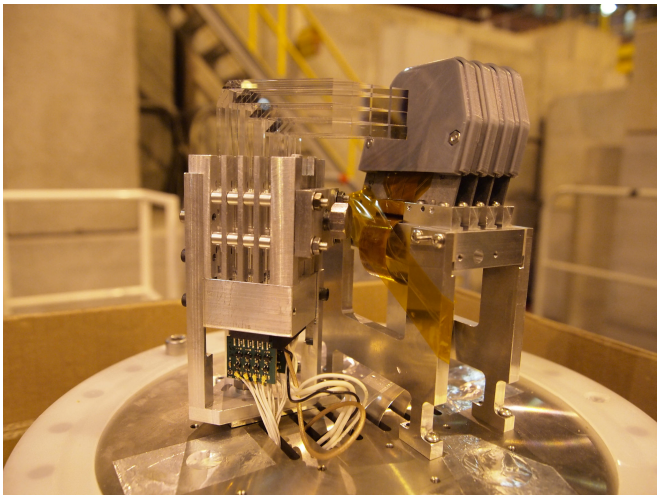

Figure 3.4: Assembled ToF detector prototype with SiT tracker planes (with protective covers) on the Roman pot flange.

For the Cherenkov light detection, the AFP ToF utilizes Photonis miniPlanacon XPM85112 [28] with the reduced anode gap for a minimal charge sharing. Active area of $25 \times 25\,\mathrm{mm}^2$ is divided into 4×4 pixels, to which the LQbars are matched. An MCP-PMT is a compact photomultiplier that uses a micro-channel plate (MCP) for electron multiplication. A schema of operation is sketched in Fig. 3.5.

An important characteristic of MCP-PMT for time of flight purposes is the time transit spread (TTS). It is the variation in signal propagation time through the MCP-PMT for the case of single photoelectron (i.e. one electron generated by a photon in the photocathode).

For a higher illumination, time resolution of MCP-PMT improves as

$$\frac{\sigma_{\mathrm{TTS}}}{\sqrt{N_{\mathrm{pe}}}} \oplus \sigma_{\mathrm{const}} \equiv \sqrt{\frac{\sigma_{\mathrm{TTS}}^2}{N_{\mathrm{pe}}} + \sigma_{\mathrm{const}}^2}, \tag{3.1}$$

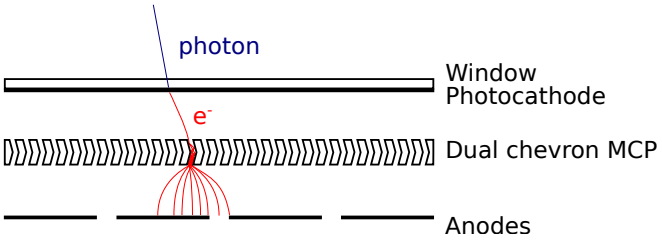

Figure 3.5: Schema of an MCP-PMT.

where N_{pe} is the mean number of produced photoelectrons and σ_{const} is contribution of an irreducible internal electronic jitter [29].

A crosstalk is also of importance in case of multi-anode MCP-PMTs. As the anodes are placed next to each other, a signal from one channel can influence measurement of neighboring channels. Two main sources of crosstalk are always present — charge sharing and capacitive coupling.

The MCP-PMT output is read out by an electronic chain designed with an aim to minimize the induced electronic jitter that affects timing performance of the ToF system. The schema of the readout chain is illustrated in Fig. 3.6. The signal is amplified by a set of broadband preamplifiers (PAs) with a variable gain up to 20 dB per stage. Next, a constant fraction discriminator (CFD) is used to obtain a sharp stable square pulse needed for a digitizer, that provides digital information to be stored. The selected digitizer is based on the HPTDC chip developed at CERN and the data acquisition (DAQ) is handled by RCE system interfaced to the central ATLAS DAQ [5, 30, 31].

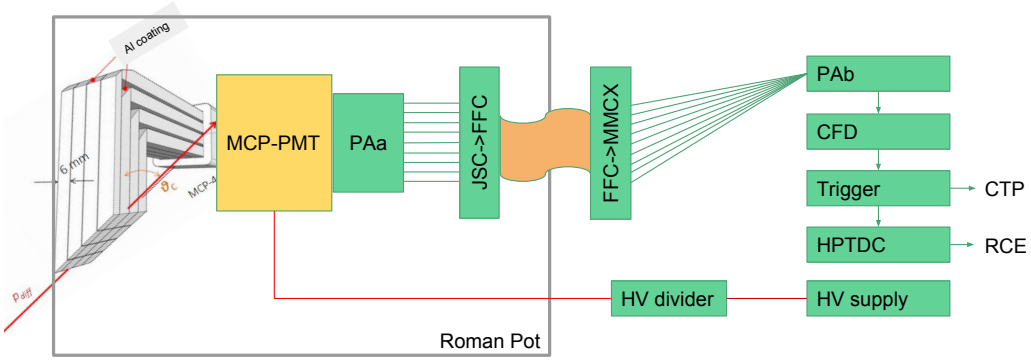

Figure 3.6: Schema of ToF readout electronics.

The PAb, CFD, trigger and HPTDC modules are installed in a NIM crate located at the foot of the AFP station base, about 1 m below the Roman pot.

3.2 Beam test campaigns

The AFP detectors were tested with a hadron beam during several beam test campaigns. At first, SiT and ToF, were tested separately and in later stages, the

full readout chain, including the RCE, was utilized and SiT and ToF detectors took combined data. All these tests took place at the CERN North Area site, at the CERN building 887. The beam was mostly composed of 120 GeV π^+ pions for the AFP beam tests.

A general measurement scheme and the experimental setup was very similar throughout all the beam tests I describe here, although parts of the setup changed as necessary for particular goals of a given beam test. An experimental setup consisting of four tracker planes, two ToF detectors and two SiPM timing reference detectors is shown in Fig. 3.7.

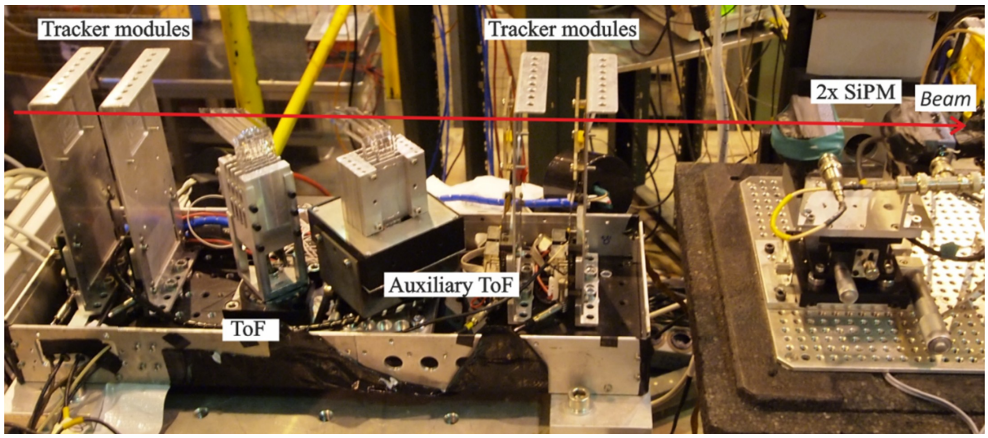

Figure 3.7: Beam test experimental setup [P14].

Various versions of ToF prototype were tested in beam tests. Main focus was on time resolution of the whole ToF system, however to optimize the resolution, it was needed to study the interplay of individual components. Different versions of bars were tested, individual bars and single trains were measured to understand crosstalk, several ToF holder designs were used, an optical separation of bars was studied and several MCP-PMTs were utilized. SiPM detectors were used as a timing reference.

A fast oscilloscope was used to capture full MCP-PMT waveforms and to measure the time resolution of ToF without the influence of the HPTDC. Only a part of the readout chain was used in such measurements. Only the PAa and PAb amplifiers were used for the measurements capturing the full waveform (so-called *raw measurements*) and the CFDs were usually added for the time resolution studies (*CFD measurements*).

The RCE was used to record both SiT and ToF data. These were used for the ToF alignment as well as measurements of timing resolution including the HPTDC contribution, efficiency of the ToF channels and their crosstalk.

3.2.1 November 2014

The first beam test I participated in, was focused on the integration of SiT and ToF readouts. The operation of the first LQbar ToF prototype, finding

the optimal operation voltage of the MCP-PMT and the first timing resolution measurement were also of great interest. Four trains consisting of two bars each were prepared by the JLO workshop, the mechanical construction by the SBU and the Photonis MCP-PMT was provided by the University of Texas in Arlington (UTA).

The beam test started by bringing all the detectors alive, locating the beam and aligning the detectors to the beam. The SiPM voltage was optimized to 30.7 V. The HV for the MCP-PMT was tuned to achieve a good separation of the signal pulses from the noise pedestal, while staying within the voltage range given by the CFD dynamic range. The optimal HV value of 1850 V was found for the tested MCP-PMT.

The integration of readout of SiT and ToF detectors using the RCE was successful and common data were taken and analyzed as illustrated in Fig. 3.8.

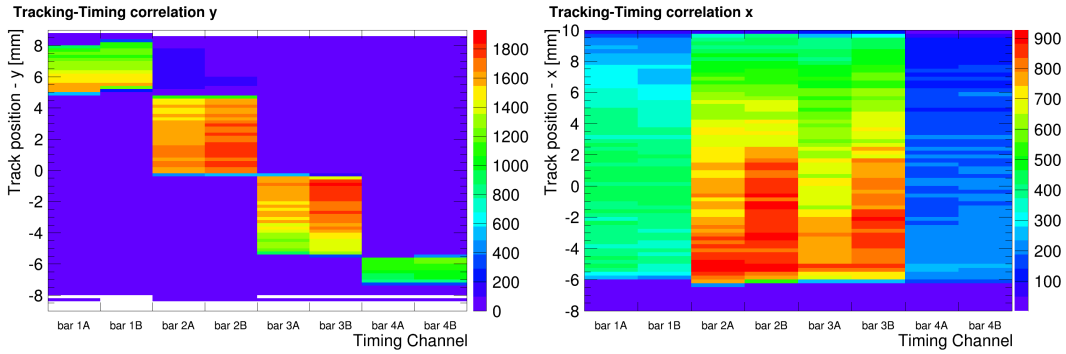

Figure 3.8: Correlation between the reconstructed SiT track position and response in ToF channels for the x (*right*) and y (*left*) coordinate. The MCP-PMT HV was set to 1800 V [P10].

The first timing results were obtained from the histograms set up in the WaveStudio control software of the oscilloscope during the CFD measurements. The full width at half maximum (FWHM) of distributions of a time difference between a bar and the triggering SiPM was measured in range 70–90 ps including the contribution of SiPM time resolution (of about 30 ps FWHM). This corresponds, for a Gaussian distribution (since FWHM $\approx 2.35\sigma$), to σ of 27–36 ps per bar with the SiPM contribution subtracted (in quadrature, assuming no correlations).

3.2.2 September 2015

The next beam test focused on tuning and measuring properties of SiT and ToF detectors. Spatial resolution of SiT was measured with 14° tilt foreseen for the final version, a range of bias voltages was tested and charge readout was tuned for the optimal resolution [P10]. The ToF was tested with a new MiniPlanacon MCP-PMT loaned to the AFP by Photonis (with the found optimal HV of

1870 V) and, for a direct comparison, also the previously used MCP-PMT from UTA was utilized. New sets of bars and options for an optical coupling of the LQbars to the MCP-PMT front face were tested as well as x dependence of time resolution.

All the LQbars were tested during the beam test in order to check how consistent is their response. One of the tests was the measurement of the pulse amplitude distribution for all the LQbars as plotted in Fig. 3.9. For this measurement, the bars were placed into the holder such that there is an empty space in between the A and B bars to reduce the light spillage from A to B bars.

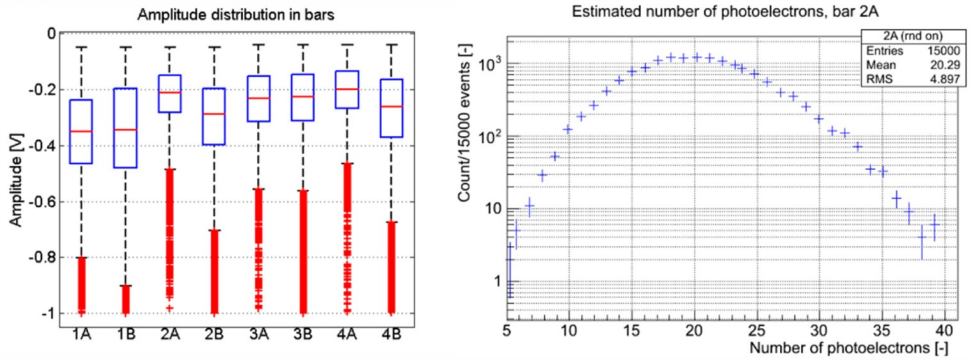

Figure 3.9: *Left:* Distribution of the amplitudes with the blue boxes representing the range from the 25 % to the 75 % quantile, the red line marking the mean value and the dotted line representing the distribution range excluding the outliers drawn as the red points. *Right:* Distribution of generated photoelectrons obtained from a Monte Carlo simulation [P3].

It is evident that the bars of the train 1 manifest larger mean amplitudes than the rest of the bars by about 30 %. This confirms the benefit of the taper.

The time resolution of all the bars was measured and the time resolutions of two bar trains were determined. The bar resolutions were obtained from the distribution of times of a pion registration in a bar with respect to the SiPM1, as illustrated in Fig. 3.10. The time distribution was fitted by a Gaussian, the width of Gaussian was extracted and the time resolution of the SiPM1 (12 ps) was subtracted in quadrature. For this measurement, the bars were placed again right next to each other.

The time resolution of a two bar train was determined from the time distribution of the averages of times determined by the two bars in the train (in each event time measured by the train is calculated as $t_{\mathrm{tr}} = \frac{1}{2}(t_{\mathrm{A}} + t_{\mathrm{B}})$).

The time resolutions were measured with the SiPM aligned with the edge (i.e. covering the $3 \times 3\,\mathrm{mm}^2$ area of the bar ranging in x from the edge to 3 mm) and the SiPM positioned 5 mm from the edge (i.e. the x range of 5–8 mm). For the SiPM at the edge, values ranged 31–34 ps for the A bars, all the B bars manifested 26 ps and the whole train resolutions were measured in range 23–27 ps. The measurement error of ± 2 ps was estimated from variation between 5 independent measurements.

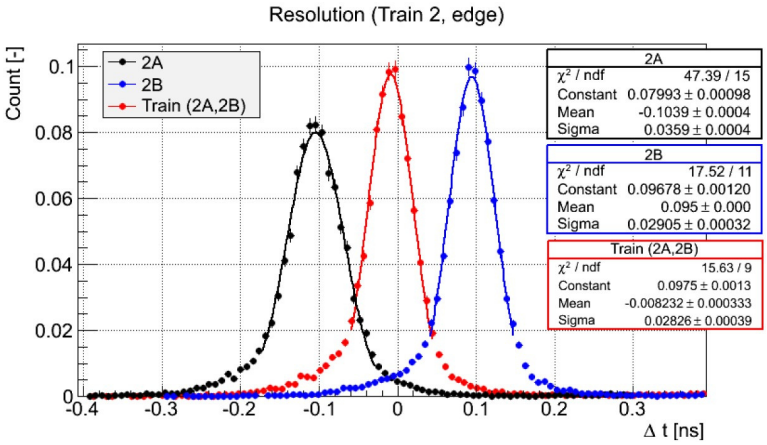

Figure 3.10: Time resolution distributions of the bars 2A and 2B, and of the two-bar train [P3].

The performance near the edge is consistently superior to the 5 mm from the edge with differences 3–10 ps. The parallel cut at the edge reflects part of the Cherenkov cone that would be lost otherwise and therefore increases light yield from a charged particle. This is effective up to about 4 mm (based on a simulation). The overall performance of the train 1 (with the taper) is better by 2–6 ps. The B bars show better time resolution both at the edge (by 5–8 ps) and at the 5 mm from the edge (by 9–13 ps). The reason for this behavior is that a part of a Cherenkov cone generated in one bar in a train leaks into the following bar in the same train.

The LQbars usually sit on top of the MCP-PMT faceplate without any optical bonding. This presents two steps in refractive index (fused silica → vacuum (air) → MCP-PMT faceplate (fused silica or borosilicate glass)) and causes that a fraction (about 4 % for the perpendicular direction) of photons is reflected on each transition. The light transmission can be improved by an optical grease with a similar refractive index as the fused silica.

Although the test with the grease (glycerol) shown significant improvement of the time resolutions, the grease was not used in further beam tests and the final detector. Reasons were mostly technical — operation of the detectors in vacuum demands use of a grease that does not evaporate or outgasses in vacuum and is radiation tolerant at the same time.

Analysis of the oscilloscope data shown large correlations between times with respect to the trigger registered by two bars of the same train. A correlation between 65–73 % was observed. In case of independent measurements, there should be no correlation.

The major part of the correlation is however caused by the time reference. What is happening is that the SiPM trigger itself is not perfect and manifests a finite time smearing (12 ps for the case of the measurement). The time fluctuation of the trigger in an event is the same for all measured channels and therefore causes a correlation. I confirmed this hypothesis using a toy simulation with the

results shown in Fig. 3.11.

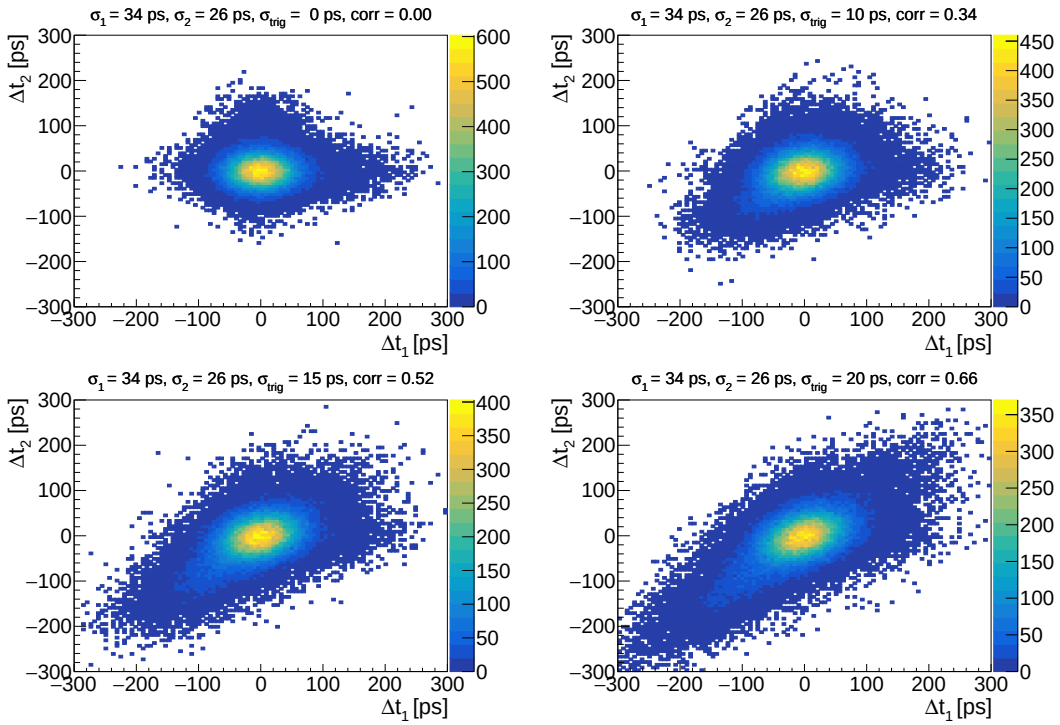

Figure 3.11: Correlation plots of simulated time distributions of two bars of a train for increasing time resolution of a trigger.

3.2.3 2016 beam tests

The year 2016 was filled with preparations for the installation of the second AFP arm and the ToF detectors. There were three ToF beam tests (in July, September and October, 5 weeks in total) and one tracker beam test (in April, one week) during this year. The tracker planes were successfully tested in their final assembly mounted on the tilted carbon fiber reinforced aluminum plates.

Full four-bar trains were tested for the first time in ToF. Also, the performance of new trains with 2 mm and 4 mm thick radiators was measured. For the purposes of the beam tests, these bars were labeled train 5 (2 mm radiator) and train 6 (4 mm), while the labels of the previously utilized trains were kept. The trains 5 and 6 were designed as replacements for the train 1 and 2, respectively.

Several bar configurations were used in the beam test to understand the obtained time resolutions with the main focus on the full four-bar train resolution. The new miniPlanacon MCP-PMT was used in the presented measurements.

The time resolutions of selected individual bars without an influence of any other bars were obtained by placing only the bar of interest into the bar holder and keeping the remaining slots empty. The measured values ranged 21–24 ps with the estimated uncertainty of ±2 ps.

The train time resolutions were determined from the time distribution of the average time measured by a train $t_{\text{avg}} = \frac{1}{4}(t_{\text{A}} + t_{\text{B}} + t_{\text{C}} + t_{\text{D}})$.

The obtained time resolutions for all the 6 trains ranged 14–15 ps at the edge and 15–17 ps at the 5 mm distance from the edge of the radiator. The trains without the taper manifest consistently worse time resolution than the ones with the taper, although within the uncertainty. The trend of worsening the time resolution further from the edge was also confirmed by scanning the distance from the edge in several steps from 0 up to 20 mm, as is shown in the left part of the Fig. 3.12.

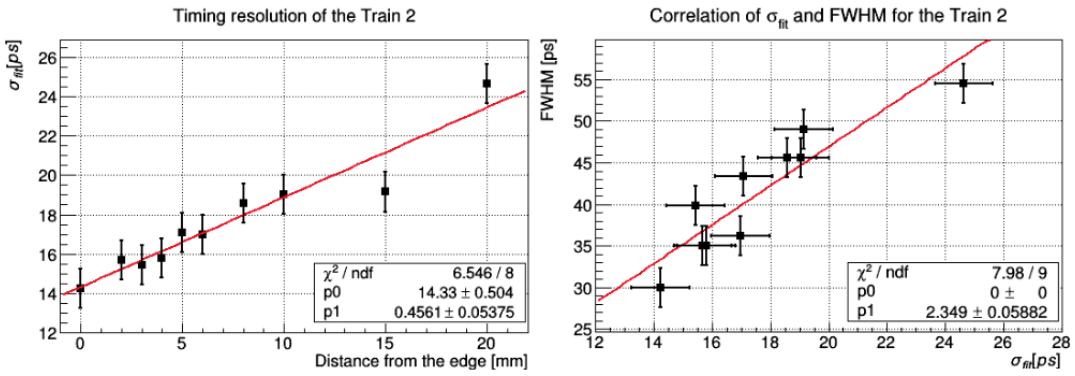

Figure 3.12: *Left:* Timing resolution of the Train 2 as a function of the distance from the edge; *right:* correlation of σ and FWHM measures of the timing resolution [P14].

The efficiencies of ToF channels were determined from the RCE data. The events with a single track in SiT were selected and the efficiency was determined as the fraction of such events with the track pointing to a given ToF channel, in which the ToF channel responded. The efficiency at the selected operating HV of the PMT (2100 V for this PMT) and the CFD threshold (−150 mV) was of the main interest and is shown in Fig. 3.13.

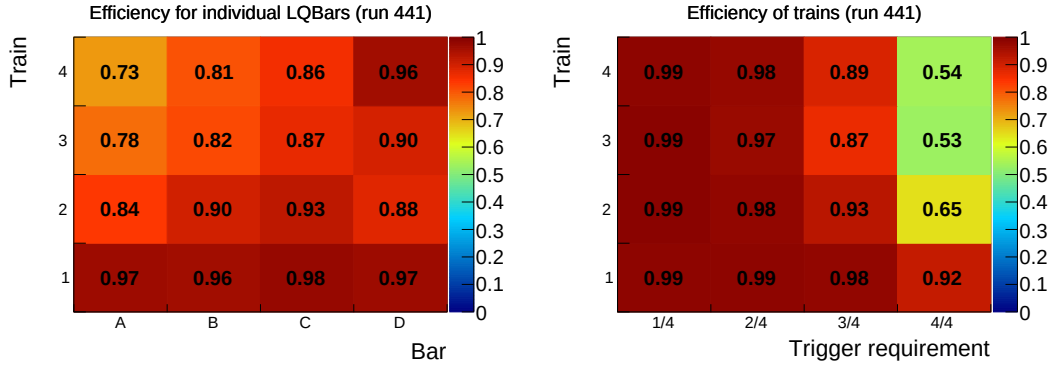

Figure 3.13: Efficiency of individual bars (*left*) and trains (*right*) for the HV of 2100 V and the CFD threshold of −150 mV.

The HPTDC contribution for individual bars was measured in range 12–17 ps. The spread of measured contributions suggests a small variance in the performance of individual HPTDC channels, however it is within the uncertainty of measurement (±2 ps).

A new SiPM was tested in the September 2016 beam test aiming to serve as an additional reference and as a spare in a case that any of the STM SiPMs would break. The new SiPM was purchased from the First Sensor company selling SiPM chips developed by Fondazione Bruno Kessler (FBK). The SiPM-NUV3S [32] chip capable of detecting light in near ultra-violet spectrum with $40 \times 40\,\mu m^2$ cell size was selected. The measured time resolution of the new SiPM was however too high: $\sigma = 70$ ps after the subtraction of the reference SiPM1 contribution.

3.2.4 2017 beam tests

The ToF detectors were installed in the LHC tunnel in April 2017 with Photonis miniPlanacon MCP-PMTs without the ALD coating with a short expected lifetime. Newly manufactured ALD coated miniPlanacon MCP-PMTs with reduced anode gap and modified internal circuitry were tested during the beam tests in July and September 2017. The circuitry modifications were done by Photonis with aim to reduce electronic crosstalk and increase signal amplitude and were based on modifications done by ALICE Fast Interaction Trigger group [33]. Also, the first prototype of trigger module was tested.

Already during the HV scan, relatively large ringing (i.e. dampened oscillations in the waveform) was observed in the trailing edge of the pulses compared to the MCP-PMT 9002053 used in the previous beam tests. The crosstalk is illustrated in Fig. 3.14. Both the new PMTs manifest higher crosstalk amplitude in the neighboring channels by up to 25 %.

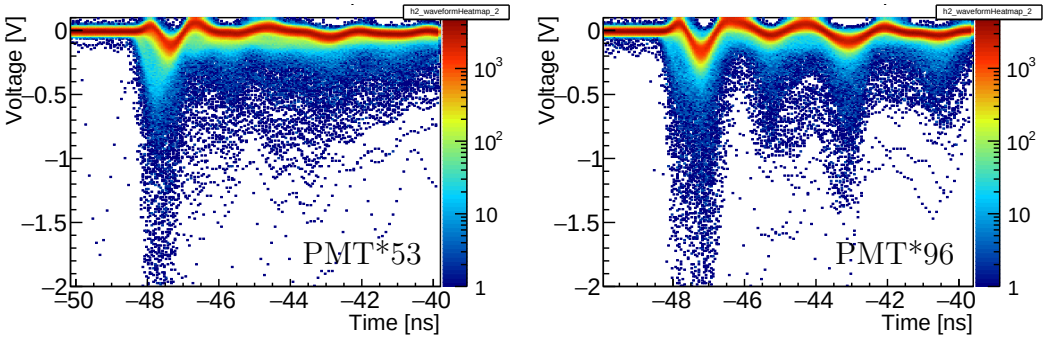

Figure 3.14: Raw crosstalk waveforms in bar 4B with signal in train 3 for MCP-PMT 9002053 (*left*) and 9002096 (*right*). There are 32768 waveforms overlaid in each plot and the color map shows the amount of overlaid waveform points.

The time resolution of the train 3 (i.e. the width of the distribution of the average from the 4 time measurements within the train) at the edge of the

parallel cut of the radiator is (27 ± 1) ps for the PMT 9002096 and (25 ± 1) ps for the PMT 9002097. The time resolutions are significantly worse from the ones measured in the beam tests in 2016. This, together with the worse crosstalk performance of the new PMTs eventually lead to replacement of the new PMTs.

The AFP ToF trigger module was tested during the July 2017 beam test. The results were not satisfactory and led to a revision of the trigger module design. It turned out that the implementation of the N/4 selection by a power combiner followed by a threshold comparator is highly temperature dependent. Temperature stabilization was implemented and the voltage thresholds for individual N/4 requirements were fine tuned.

3.3 Laser laboratory testing

The beam tests verified the performance of the whole ToF detector, comprising the LQbars, MCP-PMT detector and readout electronics. However, measurements of MCP-PMT and SiPM detectors using a controllable pulsed light source were needed to better understand contributions of individual components of the ToF system. Pulses with the width of the order of picoseconds, or narrower, were needed to characterize the detectors with time resolutions in the range 10–50 ps. The laser laboratory at the Joint Laboratory of Optics offered the possibility to perform such measurements.

In addition, an MCP-PMT illuminated by a pulsed laser provided a stable output pulses for tests of the readout electronics. A typical MCP-PMT pulse has rise time of 500 ps and width of less than 1 ns, which is beyond the capability of pulse generators commonly found in laboratories.

3.3.1 MCP-PMT characterization

The gain of MCP-PMTs usually varies significantly (even more than by a factor of 2) across the active surface [34] and manufacturers are working on improvements. As this can influence performance of individual ToF channels in terms of efficiency as well as time resolution, the uniformity of response of individual pixels was evaluated for the the MCP-PMT 9002053 before its use at the beam tests in 2016. The results are presented in Fig. 3.15.

The mean amplitude among pixels ranges 498–606 mV with mean value of 563 mV. The ratio of the minimum to the maximum mean amplitude is 1:1.22. The time resolution varies between 18–23 ps with the mean value of 21 ps. Naively, one would expect an anticorrelation between the mean amplitude and the time resolution of a pixel. This would be true for the fixed gain and varying amount of incident light, as indicated by Eq. 3.1. However in this case the amount of incident light is the same, while the gain varies. The gain can vary because of non-uniform quantum efficiency of the photocathode, which would result in varying N_{pe} and hence the anticorrelation, or because of non-uniformity at the

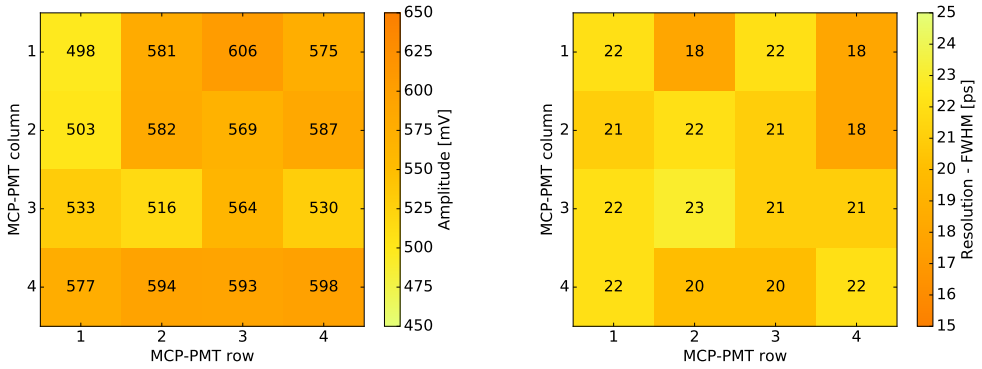

Figure 3.15: Uniformity of the MCP-PMT 9002053 response in terms of the output pulse amplitude (*left*) and the time resolution (*right*). The colormap is inverted between the two plots, as the resolution is expected to rise with decreasing amplitude.

Table 3.1: Time transit spread measurements of MCP-PMTs measured in the JLO laser lab. The estimated uncertainty is ± 2 ps.

PMT	Channel	N_{pe}	HV [V]	σ_{TTS} [ps]
XP85012 (2 inch)	54	0.1	3050	75
BT2015	12	0.05	2100	43
	13	0.05	2100	41
	22	0.05	2100	39
BT2016 (9002053)	11	0.19	2370	46
	33	0.19	2370	49

MCP layers. As the anticorrelation is not observed in Fig. 3.15, the main source of non-uniformity is likely in the MCP layers.

The time transit spread (TTS) was measured for three MCP-PMTs. The TTS is an important attribute of an MCP-PMT defining its timing performance, as discussed in Sec. 3.1. It characterizes its time resolution when only one photoelectron is produced per event.

The results for the measured channels of the three characterized MCP-PMTs, with the trigger contribution subtracted, are listed in Tab. 3.1. There are small differences between different pixels of the same MCP-PMT and the best performance is observed in the case of the PMT from the 2015 beam test. This is, at first sight, contradicting the obtained time resolutions of bars at the beam tests with the two miniPlanacon tubes, where the PMT 2002053 performed better. However, the TTS is only a part of the time performance for a given number of incident *photons*. A given number of photons is produced in an LQbar and Eq. 3.1 relates the TTS to time resolution for a given number of *photoelectrons* produced at the photocathode. The feature relating these two numbers is the quantum efficiency.

3.3.2 SiPM measurements

Silicon photomultipliers (SiPMs), or multipixel photon counters (MPPCs) as Hamamatsu calls them, are solid state detectors capable of detecting very low light down to single photon levels. An SiPM sensor is build from an array of cells, consisting of an avalanche photodiode (APD) connected in series with a quenching resistor [35, 36]. All cells are connected in parallel and provide a single output. Different SiPM models provide a sensitivity to a specific wavelength range of incident light. UV sensitive models are of interest for Cherenkov timing applications. Typically the UV sensitive SiPM provide the sensitivity in the range 300–600 nm, with the peak detection efficiency around 400 nm.

During the development of the ToF system of the AFP, a 3.5×3.5 mm^2 SiPM produced by STMicroelectronics (NRD09_1, 58×58 µm^2 cell size) coupled with a 3 cm long quartz Cherenkov radiator was utilized.

Since the STM NRD09_1 was not being produced anymore already during the first beam tests, possible replacement was investigated. I measured timing properties of SiPM detectors from the FBK and the STM producers, with a focus on the time resolution under variation of the light intensity, an over-voltage and a wavelength of the light.

Figure 3.16 plots the dependence of the time resolution on the N_{pe} and the SiPM overvoltage. Both SiPMs follow very well the $\sigma_{\text{TTS}} N_{\text{pe}}^{-\frac{1}{2}} \oplus \sigma_{\text{const}}$ behavior (the lines in the figure show the fit results). Both SiPMs show a similar behavior for the two wavelengths.

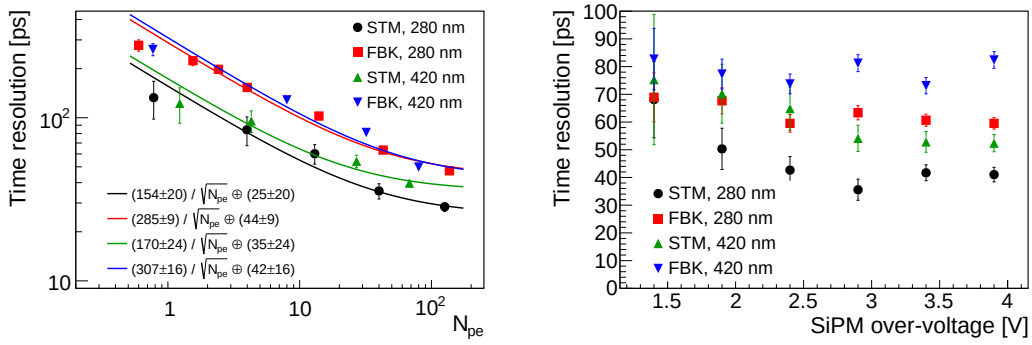

Figure 3.16: Time resolution dependence on N_{pe} for the overvoltage of 2.9 V (left); the resolution as a function of the overvoltage for N_{pe} in range 20–30 for 420 nm and 35–45 for 280 nm (right).

The devices manifested the TTS of (245 ± 10) ps (FBK) and (124 ± 22) ps (STM) and the best time resolutions, achieved for N_{pe} of the order 10^6 for 420 nm, of (8 ± 1) ps and (4 ± 1) ps for the FBK and STM SiPM, respectively.

The results for the two wavelengths were very comparable, with 280 nm providing worse results at very high illumination: (27 ± 1) ps (FBK) and (8 ± 1) ps (STM) at N_{pe} of the order 10^4.

The STM SiPM has already proved to be a great detector for Cherenkov time-of-flight systems, reaching 11 ps when combined with 3 cm quartz radiator [P10]. However, the FBK device was found to provide worse resolution by a factor of 2–3.

The worse resolution was confirmed also during a beam test, where the resolution of 70 ps was measured (see Sec. 3.2.3), exceeding the estimated resolution, likely due to worse photodetection efficiency for the UV light.

3.4 Installation and commissioning

The AFP ToF detector was installed for the first time during the year end technical stop (YETS) starting at the turn of 2016. The work on the installation finished by the end of April 2017 and the commissioning started in May 2017. I participated in the preparatory works before the installation and in the commissioning of the ToF detector.

Two ToF detectors were prepared for the installation with the newly prepared LQbars and mechanical holder construction. Two MCP-PMTs were foreseen for installation — serial number 9002053 previously tested in beam tests and a new 9002086, tested in the JLO laser laboratory by Tomáš Komárek (JLO). Both had a fused silica front window with a bi-alkali photocathode and 10 µm MCP pores.

Further tests were needed before the installation in addition to what was done during the development and in the beam tests. Signal path was validated for each ToF channel from the PAa to the HPTDC module. The PAa and PAb amplifiers, the CFD modules and the HPTDC modules produce significant amount of heat that needs to be dissipated. Heat dissipation and cooling were tested and the operation temperatures determined. The automatic interlock system was configured accordingly.

The MCP-PMT ability to operate in vacuum needed to be verified. The test was successful in case of PMT 9002086, but the PMT 9002053 failed at 2.0 kV. A pair of MCP-PMTs with a borosilicate glass window was loaned to the AFP by Photonis as a replacement and the one labeled 9002089 was installed instead of the 9002053.

The commissioning of the newly installed AFP stations and the ToF detectors started with the LHC recommissioning at the beginning of May 2017. Initially, the LHC was filled with non-colliding beams and AFP stayed in its retracted position (the so-called *garage* position) most of the time. Stable beams collisions started in the second half of May with intensity and number of bunches steadily growing till the beginning of June. By the end of June, the AFP stations were being inserted on a regular basis shortly after the start of an ATLAS run.

A clear correlation between the track position reconstructed by the SiT and the response of ToF channels was observed in the RCE data during the beam tests (as shown e.g. in Fig. 3.8). It was, therefore, expected to be seen also in the data with the LHC proton beam. However, the correlation was initially

not observed. The correlation became apparent after more restrictive cuts were applied, as illustrated in Fig. 3.17.

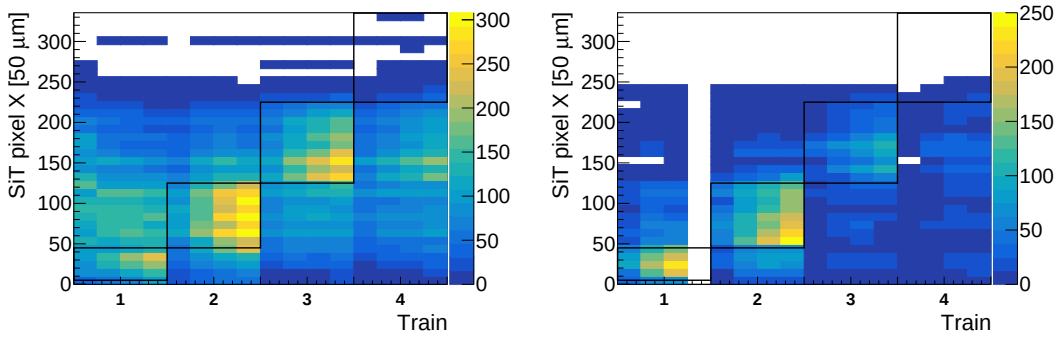

Figure 3.17: SiT-ToF correlation after TS1 with the tight selection for the A side (*left*) and the C side (*right*), run 328339. The black boxes illustrate expected signal regions.

The need for the tight selection in the SiT-ToF correlation plots also suggested that efficiency of ToF channels might have been very low. First, I used GNAM histogramming and studied the relative efficiency of the possible N/4 selections of bars within train with respect to the 1/4 selection. This did not reveal issues, however, the values were biased by the 1/4 requirement on a ToF train.

As GNAM provides only limited amount of events and it is not very straightforward to run GNAM code on already taken data, I moved to analysis of data taken in standalone mode, as soon as the reconstruction of the raw data format into the ATLAS xAOD format became available. The efficiency was calculated as the fraction of events with a clean track in the SiT (the same clean track selection as in the SiT-ToF correlation was used) having the x pixel coordinate in the defined range (bins with the width of 5 pixel rows were used in the following plots) in which a given ToF channel responded. Results for all the ToF channels in the low μ part of the run 336505 (23rd September 2017) are shown in Fig. 3.18.

The observed efficiency within the x range corresponding to bars of a given train is 5–8 % for the A side and 1–3 % for the C side. Train 4 has low statistics due to the beam profile.

The reason of the low efficiency was investigated. There were three possible explanations being considered: a deteriorated MCP-PMT gain due to collected charge, an insufficient rate capability of the MCP-PMT and a threshold inefficiency caused by a too low HV or a too high CFD threshold. The too low HV setting and by the soon reached lifetime of MCP-PMTs resulting in the deteriorated gain were identified as the causes.

Despite the low efficiency, it was possible to determine time resolutions of ToF channels. I used data from the low μ part of the run 336505 with statistics of 13 million events. The results are listed in Tab. 3.2. The missing values are

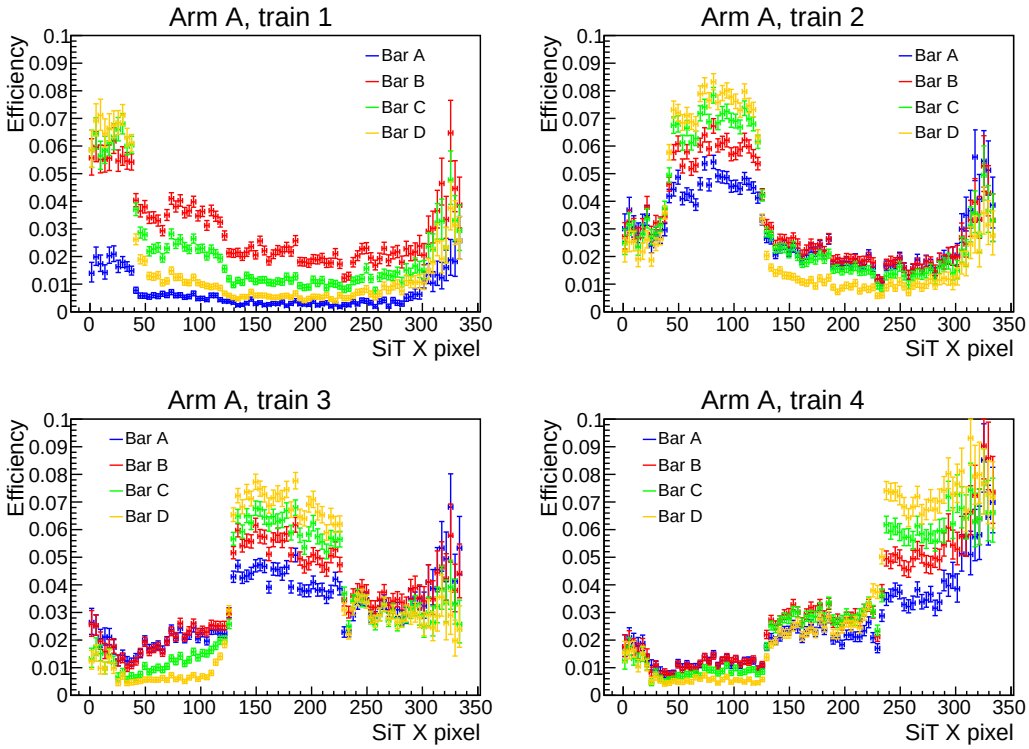

Figure 3.18: ToF efficiency as a function of SiT x coordinate in the run 336505.

caused by missing 1A on side A and 1D on side C in the data and due to failed fitting procedure in case of 1C on side A and 4C on side C. There are few very low values of time resolutions bellow 20 ps, which are contradicting the beam test results and these suggest the total systematic error of determined values to be close to 10 ps. The average time resolution is 32 ps.

Table 3.2: Resolution of bars from the LHC data in picoseconds.

	A side, bar:				C side, bar:			
Train	A	B	C	D	A	B	C	D
1	—	37	—	36	52	33	24	—
2	40	25	22	14	46	25	31	26
3	27	33	34	21	37	28	13	40
4	61	26	26	33	54	27	—	35

Conclusion

The work on this thesis comprised the software development, the data analysis, setting up and performing experiments and the detector hardware development.

The full simulation model of the ATLAS forward region was extended by orbit correctors and field transformations, further tuned and validated. The RP filler of ALFA stations was implemented.

The study of ATLAS central magnetic field influence on ALFA measurement at 7 TeV shown the effect on the four-momentum transfer t measurement of elastic protons of 0.3 % in Monte Carlo simulations. The comparison to data shown too large discrepancies between the model and the data to draw conclusions.

The simulation of multiple scattering and showers on the AFP thin entrance window demonstrated how much the tilt window, that was considered for the Hamburg beam pipe housing later replaced by Roman pots, affects the diffracted protons and AFP measurement. The scattering angle rose from 0.90–0.96 µm, for the window perpendicular to the beam, up to 1.61–1.81 µm for the window tilted at 11°. The fraction of showers was almost doubled between the two window angle limits.

The AFP ToF detector was successfully designed, manufactured and tested. Time resolution, crosstalk and efficiency of individual ToF channels were characterized.

The time resolution of ToF without the HPTDC contribution was measured and it was shown that the best achieved time resolution of individual bars was 20–30 ps. The trains with the taper manifested better time resolution by 5–15 %. The first bar within a train is always handicapped by the missing light leak that the consequent bars receive from their predecessors. The time resolution of the entire trains starts at 14–15 ps.

The best time resolutions were achieved near the edge of the parallel cut of the radiator part of a bar. The dependence of the resolution on the distance from the edge is approximately linear with e.g. the train 2 time resolution growing from 14 ps at 0 mm to 24 ps at 20 mm from the edge.

The ToF detector was integrated into the common AFP readout that uses the RCE system. The time measurements were digitized using the HPTDC module, which adds an additional smearing to the measurement. The HPTDC contribution to the time resolution was 12–17 ps. The combined ToF train resolution is therefore 15–30 ps over the AFP acceptance.

The crosstalk between bars was measured and it was shown that there is

a negligible optical crosstalk, except for the light leaking from one bar to the next within a train. Within one train, the crosstalk between channels results in a correlation of measurements in the train. The correlations of up to 20 % were observed in the RCE data (using different SiPMs as a reference for the bars being evaluated to avoid the trigger induced correlation). The crosstalk between bars of different trains reduces the ToF ability to handle a high pileup. E.g. in case of two protons in one ToF arm within an event, the time measurement of the second proton is spoiled by the first one, if the crosstalk is large, even if they hit different trains. The results for the MCP-PMT with the reduced anode gap showed up to 12 % events with the crosstalk contribution above the noise pedestal to the neighboring channel. Typically the crosstalk pulse starts in the positive voltage (opposed to the negative signal pulse) followed by several dampened oscillations with the amplitude of 8 % of the signal pulse causing it.

ToF channels manifested high efficiency of 80–98 % per bar and above 87 % efficiency when requiring 3 out of 4 bars within a train to respond. Bars with taper performed significantly better, with efficiency above 96 % per bar and 98 % for the 3/4 requirement.

The ALD coated Photonis MCP-PMTs were tested during 2017 beam tests, promising extended lifetime of about $10\,\mathrm{C\,cm^{-2}}$, corresponding to about a year of operation in the AFP [5]. These performed significantly worse with train time resolutions above 25 ps and increased crosstalk. These MCP-PMTs were not installed and they were replaced in 2018.

The measurements in the laser laboratory provided a useful insight into the MCP-PMT characteristics and performance of SiPMs. A good miniPlanacon MCP-PMT uniformity with the pixel variations in both mean signal amplitude and time resolution of less than 27 % was measured. The time transit spread, as the characteristic determining the timing performance of an MCP-PMT with a given detection efficiency, was measured in the range 39–49 ps for the channels of Photonis miniPlanacon XPM85112 tubes.

The STM and the FBK (branded as First Sensor) SiPMs were characterized with the focus on the time resolution under various illumination by two light wavelengths: 280 nm and 420 nm. The devices had the TTS of (245 ± 10) ps (FBK) and (124 ± 22) ps (STM). The time resolution dropped with increasing N_{pe} as $\sigma_{\mathrm{TTS}} N_{\mathrm{pe}}^{-\frac{1}{2}} \oplus \sigma_{\mathrm{const}}$ with the best time resolutions, achieved for N_{pe} of the order 10^6 for 420 nm, of (8 ± 1) ps and (4 ± 1) ps for the FBK and STM SiPM, respectively. The FBK SiPM was intended to serve as a replacement in case of a failure of one of the STM SiPMs. However, due to the significantly worse timing performance, confirmed also in a beam test, a different spare SiPMs had to be found. Later, the SensL MicroFC-SMA-30050 SiPMs were chosen.

The AFP ToF detectors were installed together with the second arm of AFP stations during the EYETS in the period of January–April 2017. The commissioning started at the beginning of May. ToF detectors worked, however low efficiency at the level of 1–8 % was observed. This was caused by too low HV setting and by the soon reached lifetime of MCP-PMTs. A monitoring of MCP-

PMT signal amplitude was implemented to avoid the low HV in the future. Even though the efficiency was low, the timing performance was evaluated and an average bar time resolution of 32 ps was measured, promising good prospects once the ToF is reinstalled and set up properly.

Currently, the ToF detectors are not installed in the LHC tunnel. They were removed at the end of 2017 and were not reinstalled due to the issues with the ALD coated PMTs measured in 2017 beam tests. Replacements for these tubes were obtained, however issues with operation in vacuum arose.

The AFP ToF detectors need a further development in order to keep up with the increasing luminosities in the LHC Run 3. The foreseen replacement of the HPTDC by the picoTDC should improve the $\sim$5 MHz limitation at the readout and the added PAc amplifier and the ToF shielding allows to handle higher rates due to the lowered gain of the MCP-PMT. In addition, glue-less bars are being developed at the JLO, promising about 20 % more light at the MCP-PMT window and less deterioration due to an irradiation. This could allow to reduce the MCP-PMT gain even further and to improve time resolutions. Also, the MCP-PMTs are still improving. However, the current ToF design is not the only option. Low gain avalanche detectors (LGADs) show very promising results [P13] and diamond detectors or fast silicon detectors can be an option as well, if they prove to be enough radiation tolerant.

Shrnutí v češtině

Dizertační práce dokumentuje autorovu práci na vývoji softwaru, analýze dat, přípravě a provádění laboratorních měření a na vývoji detektoru času letu.

Model pro plnou simulaci dopředné oblasti experimentu ATLAS byl rozšířen o korekční magnety a o možnost otáčení a posuvu magnetů. Model byl odladěn a validován. Model ALFA stanic byl rozšířen o tzv. „RP filler“ sloužící pro omezení indukčního ohřevu ALFA stanic.

Studie vlivu magnetického pole solenoidu detektoru ATLAS na měření ALFA detektorů při 7 TeV ukázala s využitím Monte Carlo simulace odchylku v měření přenosu čtyřhybnosti t o 0.3 %. Srovnání s daty vykazovalo příliš velké rozdíly mezi simulací a daty, aby bylo možné věrohodně prokázat vliv na naměřená data.

Simulace rozptylu a sprškek na tenkém vstupním okénku AFP ukázala míru vlivu sklonu okénka (zvažovaného u dřívé plánovaného umístění AFP detektorů v Hamburgské trubici) na diffrakční protony měřené AFP detektory. Úhel rozptylu rostl z 0.90–0.96 µm pro okénko kolmé na svazek až na 1.61–1.81 µm pro okénko skloněné pod úhlem 11°. Četnost sprškek se mezi těmito hodnotami sklonu okénka téměř zdvojnásobila.

Detektor času letu (ToF) pro AFP byl úspěšně navržen, zkonstruován a otestován. Časové rozlišení, přeslechy a účinnosti jednotlivých ToF kanálů byly naměřeny.

Časové rozlišení ToF detektoru, vyjímaje příspěvek HPTDC, bylo opakovaně měřeno při testech AFP pomocí svazku pionů. Nejlepší časové rozlišení dosažené pro jednotlivé kanály ToF se pohybovalo v rozmezí 20–30 ps. Tyčinky opatřené zkosením („taper“) na světlovodu vykazovaly lepší časové rozlišení o 5–15 %. První tyčinka je vždy znevýhodněna absencí světla pronikajícího z předchozí tyčinky v řadě. Nejlepší časové rozlišení dosažené pro jednotlivé řady („train“) tyčinek (tvořené čtyřmi tyčinkami) bylo 14–15 ps.

Nejlepších časových rozlišení bylo dosaženo na konci tyčinky, kde je tyčinka zakončena seříznutím rovnoběžným se svazkem. Závislost časového rozlišení na vzdálenosti od konce tyčinky je přibližně lineární, např. pro train 2 roste z 14 ps na konci tyčinky na 24 ps ve vzdálenosti 20 mm od konce.

ToF detektor byl úspěšně integrován do společného vyčítacího systému AFP, který využívá systém RCE. Měření času je digitalizováno pomocí HPTDC modulu, který způsobuje dodatečné rozmytí časových měření. Příspěvek HPTDC k časovému rozlišení byl určen z výsledků testů svazkem pionů na 12–17 ps. Výsledné rozlišení ToF trainu v rámci AFP akceptance se pohybuje v rozpětí

15–30 ps.

Přeslechy mezi jednotlivými ToF kanály byly měřeny a bylo demostrováno, že optické přeslechy jsou zanedbatelné, vyjma průniku světla z jedné tyčinky do následující v rámci trainu. Přeslechy mezi kanály jednoho trainu vedou ke korelaci měřené v tomto trainu. V RCE datech byla pozorována korelace až 20 % (s využitím odlišných referenčních SiPM detektorů pro každý z vyhodnocovaných ToF kanálů, aby nevznikla korelace způsobená společnou referencí). Přeslechy mezi tyčinkami různých trainů snižují schopnost ToF systému zvládat mnohočetné interakce („pileup“). Měření MCP-PMT se sníženou anodovou mezerou prokázaly až 12 % událostí s přeslechem v sousedním kanále na úrovni převyšující práh šumu. Typický pulz vzniklý přeslechem začíná zákmitem do kladných hodnot (narozdíl od záporného pulzu pro světelný signál) následovaným několika tlumenými kmity s počáteční amplitudou odpovídající 8 % amplitudy signálového pulzu, který přeslech způsobil.

Kanály ToF detektoru prokázaly vysokou detekční účinnost 80–98 % pro jednotlivé kanály a přes 87 %, pokud požadujeme odezvu 3 ze 4 kanálů v trainu. Tyčinky se zkosením fungovaly podstatně lépe, s účinností přes 96 % na kanál a 98 % pro výběr 3/4.

Během testů se svazkem pionů v roce 2017 byly testovány nové MCP-PMT od Photonisu s ALD vrstvou, slibující prodlouženou životnost až na přibližně $10\,\mathrm{C\,cm^{-2}}$, což odpovídá přibližně ročnímu provozu AFP [5]. Tyto fotonásobiče vykazovaly výrazně horší výsledky – časové rozlišení trainu přes 25 ps a zvýšenou míru přeslechů, proto nebyly instalovány a v roce 2018 byly vyměněny.

Měření v laserové laboratoři poskytla užitečný náhled na charakteristiky MCP-PMT a SiPM detektorů. MCP-PMT miniPlanacon vykázaly dobrou uniformitu odezvy jak z hlediska amplitudy signálu, tak časového rozlišení, s variací v obou případech pod 27 %. Časové rozlišení na jednofotonové úrovní (TTS) bylo naměřeno v rozmezí 39–49 ps pro různé kanály fotonásobičů Photonis miniPlanacon XPM85112.

SiPM detektory od výrobců STM a FBK byly charakterizovány se zaměřením na časové rozlišeni při různých intenzitách osvitu na dvou vlnových délkách: 280 nm a 420 nm. SiPM prokázaly TTS (245 ± 10) ps (FBK) a (124 ± 22) ps (STM). Časové rozlišení klesalo s rostoucím středním počtem fotoelektronů N_{pe} dle $\sigma_{\mathrm{TTS}} N_{\mathrm{pe}}^{-\frac{1}{2}} \oplus \sigma_{\mathrm{const}}$ a nejlepší časové rozlišení bylo dosaženo pro N_{pe} v řádu 10^6 na 420 nm s hodnotami (8 ± 1) ps (FBK) a (4 ± 1) ps (STM). SiPM od FBK bylo zamýšlené jako náhrada pro případ selhání jednoho z dosud používaných SiPM od STM. Nicméně, kvůli výrazně horšímu časovému rozlišení, které bylo potvrzené i během testů se svazkem pionů, bylo nutné najít jinou náhradu. Později byly vybrány SiPM čipy SensL MicroFC-SMA-30050.

AFP ToF detektory byly instalovány spolu se zbývajícími AFP stanicemi během odstávky LHC v lednu–dubnu 2017. Uvedení do provozu započalo začátkem května. ToF detektory fungovaly, ale vykazovaly nízkou detekční účinnost na úrovni 1–8 %, zapříčiněnou zpočátku příliš nízkým nastavením vysokého napětí pro MCP-PMT a brzy dosaženým koncem životnosti MCP-PMT fotoná-

sobičů. Aby se v budoucnu předešlo chybnému nastavení vysokého napětí, byla implementována procedura pro monitorování amplitudy MCP-PMT pulzů. I přes nízkou účinnost bylo možné vyhodnotit časové rozlišení ToF detektorů s průměrnou hodnotou 32 ps, slibující nadějné vyhlídky pro budoucí reinstalaci ToF detektorů.

Aktuálně nejsou ToF detektory instalovány v LHC tunelu. K jejich vyjmutí došlo na konci roku 2017 a vzhledem k problémům s fotonásobiči s ALD vrstvou, které vyvstaly během testů na svazku během roku 2017, nebyly následně vráceny. I když se podařilo sehnat náhradní fotonásobiče, ukázalo se, že není možné je provozovat ve vakuu.

Další vývoj ToF detektorů pro AFP je nezbytný pro jejich fungování při zvýšené luminozitě LHC plánované po nastávající dvouleté odstávce. Plánované nahrazení HPTDC za připravované picoTDC by mělo zvýšit současné omezení $\sim$5 MHz frekvence vyčítání a přidané PAc zesilovače a stínění ToF detektorů by měly zvýšit frekvenci, kterou je schopné zvládat MCP-PMT díky provozu na nižším zesílení. Na SLO připravované bezlepidlové tyčinky by navíc měly zvýšit světelný zisk o přibližně 20 % a být odolnější vůči radiaci. To by umožnilo další snížení zisku MCP-PMT a navíc vedlo ke zlepšení časového rozlišení. A výrobci MCP-PMT také pracují na zlepšeních. Nicméně, aktuální podoba ToF detektoru není jediným možným řešením. Polovodičové detektory (LGAD [P13] a „fast silicon detectors“) nebo diamantové detektory mohou být zajímavými kandidáty, pokud prokáží dostatečnou radiační odolnost.

Appendix A

List of abbreviations

AFP ATLAS Forward Proton

ALD atomic layer deposition

ALFA Absolute Luminosity for ATLAS

APD avalanche photodiode

ATLAS A Toroidal LHC Apparatus

BD breakdown (of an APD or an SiPM)

BT beam test

BX bunch crossing (25 ns)

CD central diffraction

CEP central exclusive production

CERN European Laboratory for Nuclear Research

CFD constant fraction discriminator

CNM Centro Nacional de Microelectronica, Barcelona, Spain

CSC Cathode Strip Chamber

CTP Central Trigger Processor (of ATLAS)

DAQ data acquisition

DCS Detector Control System (of ATLAS)

DD double diffractive dissociation (double diffraction)

DDIS diffractive deep inelastic scattering

DPDF diffractive parton distribution function

DPE double pomeron exchange

DUT device under test

EM electro-magnetic

EYETS extended year end technical stop (of the LHC)

FBK Fondazione Bruno Kessler, Trento, Italy

FFC flat flexible cable

FPGA field-programmable gate array

FWHM full width at half maximum

HPTDC High Performance Time-to-Digital Converter

IBL Insertable B-layer

IP interaction point

JLO Joint Laboratory of Optics of Palacký University in Olomouc and Institute of Physics of the Czech Academy of Sciences

LAr liquid argon

LGAD low gain avalanche detectors

LHC Large Hadron Collider

LRG large rapidity gap

LS1 Long Shutdown 1 (of the LHC)

LS2 Long Shutdown 2 (of the LHC)

LSS1 Long Straight Section 1 (LHC section surrounding ATLAS)

LUCID Luminosity measurement using Cherenkov Integrating Detector

MAPMT multiple anode photomultiplier

MCP-PMT micro-channel plate photomultiplier

MD main detector (of ALFA)

MDT Monitored Drift Tube

MPPC multipixel photon counter

NTC negative temperature coefficient thermistor

OD overlap detector (of ALFA)

PAa first-stage pre-amplifier

PAb second-stage pre-amplifier

PAc third-stage pre-amplifier

pQCD perturbative quantum chromodynamics

PS Proton Synchrotron

QCD quantum chromodynamics

RCE Reconfigurable Cluster Element (a DAQ system)

RF radio-frequency

RP Roman pot

RPC resistive plate chamber

SBU Stony Brook University

SD single diffractive dissociation (single diffraction)

SiPM silicon photo-multiplier

SiT silicon tracker

SLAC Stanford Linear Accelerator Complex

SPS Super Proton Synchrotron

SPTR single photon time resolution

STM STMicroelectronics

TAN Target Absorber Neutral

TGC thin gap chamber

ToF time-of-flight

ToT time over threshold

TRT Transition Radiation Tracker

TS1 technical stop 1 (the first technical stop of the LHC in a given year)

TTS time transit spread

UTA University of Texas in Arlington

YETS year end technical stop (of the LHC)

ZDC Zero Degree Calorimeter

References

[1] ATLAS Collaboration. The ATLAS Experiment at the CERN Large Hadron Collider. *Journal of Instrumentation*. 2008, vol. 3, no. 08, pp. S08003. Available also from WWW: ⟨http://stacks.iop.org/1748-0221/3/i=08/a=S08003⟩.

[2] Evans, L.; Bryant, P. LHC Machine. *Journal of Instrumentation*. 2008, vol. 3, no. 08, pp. S08001. Available also from WWW: ⟨http://stacks.iop.org/1748-0221/3/i=08/a=S08001⟩.

[3] R. D. Heuer. *General Meeting January 2013* [online]. 2013 [visited on 2018-06-01]. Available from WWW: ⟨https://indico.cern.ch/event/219327/attachments/355208/494765/address-Jan2013.pdf⟩.

[4] F. Gianotti. *New Year Presentation* [online]. 2018 [visited on 2018-06-01]. Available from WWW: ⟨https://indico.cern.ch/event/660352/attachments/1583505/2502838/Jan-2018-talk.pdf⟩.

[5] Adamczyk, L.; Banaś, E.; Brandt, A., et al. *Technical Design Report for the ATLAS Forward Proton Detector*. 2015. Available also from WWW: ⟨https://cds.cern.ch/record/2017378⟩.

[6] *AFP Figures, twiki page*. [online]. [visited on 2018-06-01]. Available from WWW: ⟨https://twiki.cern.ch/twiki/bin/view/Atlas/AFP_Figures⟩.

[7] Barone, V.; Predazzi, E. *High-Energy Particle Diffraction*. Berlin Heidelberg: Springer-Verlag, 2002. Texts and Monographs in Physics. Available also from WWW: ⟨http://www-spires.fnal.gov/spires/find/books/www?cl=QC794.6.C6B37::2002⟩. ISBN 3540421076.

[8] Arneodo, M.; Diehl, M. Diffraction for non-believers. In. *HERA and the LHC: A Workshop on the implications of HERA for LHC physics. Proceedings, Part B*. 2005, pp. 425–446. Available also from WWW: ⟨arXiv: hep-ph/0511047 (hep-ph)⟩.

[9] Kepka, O; Royon, C; Schoeffel, L, et al. *Physics Cases within the AFP project*. 2012. ATLAS note to be made public. Available also from WWW: ⟨https://cds.cern.ch/record/1454194⟩.

[10] Fichet, S.; Gersdorff, G. von; Kepka, O., et al. Probing new physics in diphoton production with proton tagging at the Large Hadron Collider. *Phys. Rev.* 2014, vol. D89, pp. 114004. Available also from WWW: ⟨http://dx.doi.org/10.1103/PhysRevD.89.114004arXiv: 1312.5153 (hep-ph)⟩.

[11] Agostinelli, S. et al. GEANT4: A Simulation toolkit. *Nucl. Instrum. Meth.* 2003, vol. A506, pp. 250–303. Available also from WWW: ⟨http://dx.doi.org/10.1016/S0168-9002(03)01368-8⟩.

[12] *Twiki page for ATLAS ForwardTransport*. [online]. [visited on 2018-06-01]. Available from WWW: ⟨https://twiki.cern.ch/twiki/bin/viewauth/Atlas/ForwardTransport⟩.

[13] Pelikan, D.; Pfeiffer, F.; Stenzel, H. *Beam transport simulation of elastically scattered protons in Athena*. 2010. Approval request after note revision. Available also from WWW: ⟨https://cds.cern.ch/record/1240360⟩.

[14] Bussey, P.; Sherwood, P. *FPTracker package* [online]. [visited on 2018-06-01]. Available from WWW: ⟨https://svnweb.cern.ch/trac/atlasoff/browser/ForwardDetectors/FPTracker⟩.

[15] Carquin, E. et al. *FNTracker package* [online]. [visited on 2018-06-01]. Available from WWW: ⟨https://svnweb.cern.ch/trac/atlasoff/browser/ForwardDetectors/FNTracker⟩.

[16] Boudreau, J.; Tsulaia, V. The GeoModel toolkit for detector description. In. *Computing in high energy physics and nuclear physics. Proceedings, Conference, CHEP'04, Interlaken, Switzerland, September 27-October 1, 2004*. 2005, pp. 353–356. Available also from WWW: ⟨http://doc.cern.ch/yellowrep/2005/2005-002/p353.pdf⟩.

[17] *AGDD volume types*. [online]. [visited on 2018-06-01]. Available from WWW: ⟨https://twiki.cern.ch/twiki/bin/viewauth/Atlas/AGDDVolumeTypes⟩.

[18] *Virtual Point 1*. [online]. [visited on 2018-06-01]. Available from WWW: ⟨https://atlas-vp1.web.cern.ch/atlas-vp1/home/⟩.

[19] Baranov, S; Bosman, M; Dawson, I, et al. *Estimation of Radiation Background, Impact on Detectors, Activation and Shielding Optimization in ATLAS*. 2005. Available also from WWW: ⟨https://cds.cern.ch/record/814823⟩.

[20] *MAD-X — Methodical Accelerator Design*. [online]. [visited on 2018-06-01]. Available from WWW: ⟨http://madx.web.cern.ch/madx/⟩.

[21] Kittelmann, T.; Tsulaia, V.; Boudreau, J.; Moyse, E. The Virtual Point 1 event display for the ATLAS experiment. *Journal of Physics: Conference Series*. 2010, vol. 219, no. 3, pp. 032012. Available also from WWW: ⟨http://stacks.iop.org/1742-6596/219/i=3/a=032012⟩.

[22] Keck, T. *Background Simulation* [online]. 2013 [visited on 2018-09-01]. presentation on ALFA Physics meeting⟨https://indico.cern.ch/event/266616/contributions/1603083/attachments/476035/658762/thomas_keck_background_simulation_final.pdf⟩.

[23] Aleksa, M; Bergsma, F; Giudici, P -A, et al. Measurement of the ATLAS solenoid magnetic field. *Journal of Instrumentation*. 2008, vol. 3, no. 04, pp. P04003. Available also from WWW: ⟨http://stacks.iop.org/1748-0221/3/i=04/a=P04003⟩.

[24] Brandt, A.; Bruschi, M.; Bussey, P., et al. *AFP progress report*. 2013. Available also from WWW: ⟨https://cds.cern.ch/record/1595300⟩.

[25] Pinfold, J. *AFP-QUARTIC Mechanics* [online]. 2012 [visited on 2018-07-03]. Presentation on AFP review. Available from WWW: ⟨https://indico.cern.ch/event/206644/contributions/1495802/⟩.

[26] Čerenkov, P. A. Visible Radiation Produced by Electrons Moving in a Medium with Velocities Exceeding that of Light. *Phys. Rev.* 1937, vol. 52, pp. 378–379. Available also from WWW: ⟨https://link.aps.org/doi/10.1103/PhysRev.52.378⟩.

[27] *Epotek 305 datasheet*.

[28] *miniPLANACON XPM85112*. 2014. Available also from WWW: ⟨https://www.photonis.com/uploads/datasheet/pd/Mini-PLANACON-4x4-datasheet.pdf⟩.

[29] Va'vra, J.; Ertley, C.; Leith, D.W.G.S.; Ratcliff, B.; Schwiening, J. A high-resolution TOF detector—A possible way to compete with a RICH detector. *Nuclear Instruments and Methods in Physics Research Section A: Accelerators, Spectrometers, Detectors and Associated Equipment*. 2008, vol. 595, no. 1, pp. 270–273. RICH 2007. Available also from WWW: ⟨http://www.sciencedirect.com/science/article/pii/S0168900208009947⟩. ISSN 0168-9002.

[30] Rijssenbeek, M.; AFP Collaboration, et al. ATLAS Forward Proton Detectors: Time-of-Flight Electronics. *Acta Phys. Pol. B Proc. Suppl.* 2014, vol. 7.

[31] Mota, M.; Christiansen, J.; Debieux, S., et al. A flexible multi-channel high-resolution time-to-digital converter ASIC. In. *2000 IEEE Nuclear Science Symposium. Conference Record (Cat. No.00CH37149)*. 2000, pp. 9/155–9/159 vol.2. Available also from WWW: ⟨http://dx.doi.org/10.1109/NSSMIC.2000.949889⟩.

[32] *Near Ultraviolet (NUV) SiPMs*. 2015. Available also from WWW: ⟨http://www.first-sensor.com/cms/upload/datasheets/SiPM-NUV_501628.pdf⟩.

[33] Finogeev, D. A.; Grigoriev, V. A.; Kaplin, V. A., et al. Performance study of the fast timing Cherenkov detector based on a microchannel plate PMT. *Journal of Physics: Conference Series*. 2017, vol. 798, no. 1, pp. 012168. Available also from WWW: ⟨http://stacks.iop.org/1742-6596/798/i=1/a=012168⟩.

[34] Lehmann, A.; Britting, A.; Cowie, E., et al. Systematic studies of micro-channel plate PMTs. *Nuclear Instruments and Methods in Physics Research Section A: Accelerators, Spectrometers, Detectors and Associated Equipment*. 2011, vol. 639, no. 1, pp. 144–147. Proceedings of the Seventh International Workshop on Ring Imaging Cherenkov Detectors. Available also from WWW: ⟨http://www.sciencedirect.com/science/article/pii/S0168900210020954⟩. ISSN 0168-9002.

[35] Piatek, S. *What is an SiPM and how does it work?* 2016. Available also from WWW: ⟨https://hub.hamamatsu.com/us/en/technical-note/how-sipm-works/index.html⟩.

[36] Ghassemi, A.; Sato, K.; Kobayashi, K. *MPPC*. 2016. Available also from WWW: ⟨https://hub.hamamatsu.com/resources/pdf/ssd/mppc_kapd9005e.pdf⟩.

Publications

[P1] Chytka, L.; ATLAS Collaboration. Status of the ATLAS Forward Physics (AFP) project. *AIP Conference Proceedings*. 2013, vol. 1523, no. 1, pp. 316–319. Available also from WWW: ⟨https://aip.scitation.org/doi/abs/10.1063/1.4802176⟩.

[P2] Bussey, P.; Chytka, L.; Staszewski, R.; Sykora, T.; Trzebinski, M. *LHC and ATLAS Coordinate Conventions*. 2013. ATLAS internal note. Available also from WWW: ⟨https://cds.cern.ch/record/1596453⟩.

[P3] Nozka, L.; Brandt, A.; Chytka, L., et al. Design of Cherenkov bars for the optical part of the time-of-flight detector in Geant4. *Opt. Express*. 2014, vol. 22, no. 23, pp. 28984–28996. Available also from WWW: ⟨http://www.opticsexpress.org/abstract.cfm?URI=oe-22-23-28984⟩.

[P4] Cavalier, S.; Chytka, L.; Fassnacht, P., et al. *Measurement of the total cross section from elastic scattering in pp collisons at $\sqrt{s} = 7$ TeV with the ATLAS detector*. 2014. Internal draft of publication. Available also from WWW: ⟨https://cds.cern.ch/record/1700047⟩.

[P5] ATLAS Collaboration. Measurement of the total cross section from elastic scattering in pp collisions at $\sqrt{s} = 7$ TeV with the ATLAS detector. *Nuclear Physics B*. 2014, vol. 889, pp. 486–548. Available also from WWW: ⟨http://www.sciencedirect.com/science/article/pii/S0550321314003253⟩. ISSN 0550-3213.

[P6] *Full Simulation of the ATLAS Forward Region TWiki page*. [online]. [visited on 2018-06-01]. Available from WWW: ⟨https://twiki.cern.ch/twiki/bin/viewauth/Atlas/FullSimulationATLASForwardRegion⟩.

[P7] Chytka, L.; Moraa, K. D.; Sykora, R.; Sykora, T. *Full Geant4 simulation of the ATLAS forward region under the Athena framework*. 2016. Approved ATLAS note. Available also from WWW: ⟨https://cds.cern.ch/record/2239159⟩.

[P8] ATLAS Collaboration. Measurement of the total cross section from elastic scattering in pp collisions at $\sqrt{s} = 8$ TeV with the ATLAS detector. *Physics Letters B*. 2016, vol. 761, pp. 158–178. Available also from WWW: ⟨https://www.sciencedirect.com/science/article/pii/S0370269316304403⟩. ISSN 0370-2693.

[P9] Nozka, L.; Adamczyk, L.; Chytka, L., et al. Construction of the optical part of a time-of-flight detector prototype for the AFP detector. *Opt. Express*. 2016, vol. 24, no. 24, pp. 27951–27960. Available also from WWW: ⟨http://www.opticsexpress.org/abstract.cfm?URI=oe-24-24-27951⟩.

[P10] Lange, J.; Adamczyk, L.; Chytka, L., et al. Beam tests of an integrated prototype of the ATLAS Forward Proton detector. *Journal of Instrumentation*. 2016, vol. 11, no. 09, pp. P09005. Available also from WWW: ⟨http://stacks.iop.org/1748-0221/11/i=09/a=P09005⟩.

[P11] Khalek, S. Abdel; Allongue, B.; Anghinolfi, F., et al. The ALFA Roman Pot detectors of ATLAS. *Journal of Instrumentation*. 2016, vol. 11, no. 11, pp. P11013. Available also from WWW: ⟨http://stacks.iop.org/1748-0221/11/i=11/a=P11013⟩.

[P12] Pácalt, J.; Chytka, L.; Kvita, J.; Palička, J. Měření doby života mionů z kosmického záření. *Jemná mechanika a optika*. 2017, vol. 62, no. 3, pp. 84–86. ISSN 0447-6441.

[P13] Lange, J.; Carulla, M.; Chytka, L., et al. Gain and time resolution of 45 μm thin Low Gain Avalanche Detectors before and after irradiation up to a fluence of 10^{15} n_{eq}/cm^2. *Journal of Instrumentation*. 2017, vol. 12, no. 05, pp. P05003. Available also from WWW: ⟨http://stacks.iop.org/1748-0221/12/i=05/a=P05003⟩.

[P14] Chytka, L.; Avoni, G.; Brandt, A., et al. Timing resolution studies of the optical part of the AFP Time-of-flight detector. *Opt. Express*. 2018, vol. 26, no. 7, pp. 8028–8039. Available also from WWW: ⟨http://www.opticsexpress.org/abstract.cfm?URI=oe-26-7-8028⟩.

[P15] Chytka, L.; Hrabovsky, M.; Komarek, T., et al. Time resolution of the SiPM-NUV3S. Submitted to Nucl. Inst. Meth. A.

[P16] Chytka, L.; Komárek, T.; Nožka, L.; Sýkora, T.; Urbášek, V. Noise influence on time resolution of SiPM photodetectors. *Jemná mechanika a optika*. Accepted for publication. ISSN 0447-6441.